To cite this version :

Ibtissam HANOUN, George CHATZIGEORGIOU, Fodil MERAGHNI - Hierarchical micromechanical modeling for CNT-coated fuzzy fiber composites accounting for viscoplasticity and interfacial damage - International Journal of Solids and Structures p.113409 - 2025

Hierarchical micromechanical modeling for CNT-coated fuzzy fiber composites accounting for viscoplasticity and interfacial damage

Ibtissam Hanoun, George Chatzigeorgiou, Fodil Meraghni

PII: S0020-7683(25)00195-7
DOI: https://doi.org/10.1016/j.ijsolstr.2025.113409
Reference: SAS 113409

To appear in: *International Journal of Solids and Structures*

Received date : 26 February 2025
Revised date : 15 April 2025
Accepted date : 22 April 2025

Please cite this article as: I. Hanoun, G. Chatzigeorgiou and F. Meraghni, Hierarchical micromechanical modeling for CNT-coated fuzzy fiber composites accounting for viscoplasticity and interfacial damage. *International Journal of Solids and Structures* (2025), doi: https://doi.org/10.1016/j.ijsolstr.2025.113409.

Hierarchical micromechanical modeling for CNT-coated fuzzy fiber composites accounting for viscoplasticity and interfacial damage

Ibtissam Hanoun[a], George Chatzigeorgiou[a,*], Fodil Meraghni[a]

[a] *Arts et Métiers Institute of Technology, CNRS, Université de Lorraine, LEM3-UMR7239, F-57070 Metz, France*

Abstract

This study investigates fuzzy fiber composites, characterized by a viscoplastic matrix and fuzzy fibers, i.e. fibers coated with radially aligned carbon nanotubes (CNTs). A comprehensive micromechanical framework is developed to model and optimize these composites, with a particular emphasis on interfacial damage mechanisms introduced through microvoids growth in the region between the fuzzy fibers and the matrix. By developing an equivalent fiber model, the complexity of the multi-phase structure is effectively reduced, facilitating efficient parametric analyses. Various homogenization techniques, including Composite Cylinder Assemblage (CCA), Transformation Field Analysis (TFA), and periodic homogenization, are combined to predict the overall stress-strain responses of the equivalent fiber approach and then the full fuzzy fiber composite. The identification of the framework and model parameters enabled a parametric/sensitivity analysis to study the

---

*Corresponding author.

Email addresses: `ibtissam.hanoun@ensam.eu` (Ibtissam Hanoun), `georges.chatzigeorgiou@ensam.eu` (George Chatzigeorgiou), `fodil.meraghni@ensam.eu` (Fodil Meraghni)

Preprint submitted to Elsevier *April 15, 2025*

effect of varying key parameters, including the volume fraction. The results of this paper contribute to a deeper understanding of unidirectional fuzzy fiber composites and establish a foundation for future parametric investigations and fuzzy fiber composite applications accounting for nonlinear regimes.

Keywords: Fuzzy fiber composites; carbon nanotubes; homogenization; viscoplasticity; composite cylinders assemblage; transformation field analysis; effective properties; inelastic mechanisms, interfacial damage.

1. Introduction

Carbon nanotubes (CNTs) were first discovered in 1991 by Iijima [1], and since then they have attracted increasing attention in recent decades due to their exceptional mechanical and thermal properties ([2], [3], [4], [5]). Their unique structure, composed of rolled graphene sheets (Figure 1), gives CNTs high mechanical strength, remarkable electrical conductivity, and light weight ([6], [7]). These characteristics make them promising candidates for a wide range of applications, from advanced structural composites to electronic devices [8].

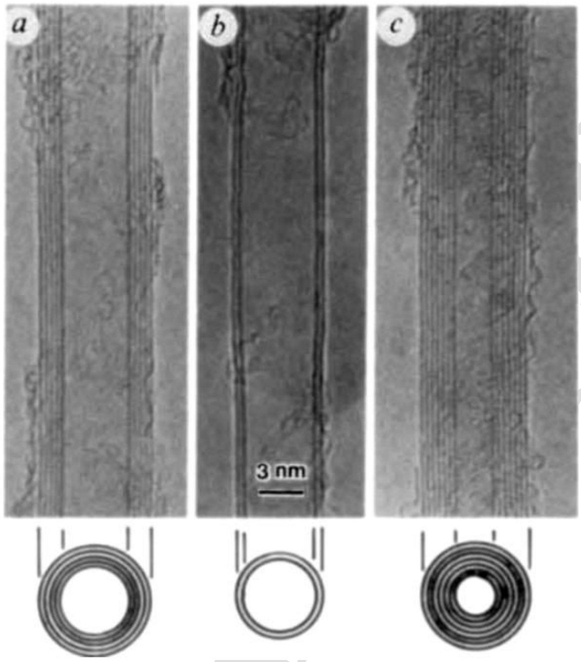

Figure 1: TEM image of microtubules of graphitic carbon (nanotubes). Parallel dark lines correspond to the lattice images of graphite. A cross-section of each tubule is illustrated. a) Tube consisting of five graphitic sheets, diameter 6.7 nm. (b) Two-sheet tube, diameter 5.5 nm. (c) Seven-sheet tube, diameter 6.5 nm, which has the smallest hollow diameter (2.2 nm). This figure is taken from Nature journal by Iijima [1].

An innovative method in composite materials involves the creation of "Fuzzy Fibers" by grafting carbon nanotubes (CNTs) on the fiber surfaces using chemical vapor deposition [9]. This technique seeks to enhance interfacial strength and stiffness, setting the stage for the next generation of high-performance composites [10]. Carbon nanotubes (CNTs), which can exist in either straight or wavy forms, are the focus of a study that examines the specific influence of wavy CNTs in fuzzy fiber reinforced composites, considering their interaction with two-scale interphase effects on the material's mechanical properties [11].

The incorporation of carbon nanotubes (CNTs) on the circumferential surfaces of conventional fibers further amplifies the benefits, offering significant advantages such as enhanced fiber-matrix interface through multiple synergistic mechanisms, as well as enhanced mechanical strength and toughness due to improved load transfer. By creating nano-scale surface roughness, CNTs increase the contact area and mechanical interlocking with the polymer matrix, optimizing stress transfer. This configuration also introduces additional electrical conductivity, while improving thermal management for high temperature applications. Additionally, the CNT-coated fibers remain lightweight yet damage-resistant, protecting against wear and microcracks.

Many theoretical models have been conducted to identify and understand the mechanical behavior of fuzzy fiber composites, including their elastic properties ([12], [2], [10]), elasto-plastic ([13], [14]), thermoelastic ([15], [16]) and electromechanical ([17], [18]). In addition to experimental investigations, the growing application and development of novel fuzzy fiber composites and their structural components have stimulated a new field of research within the simulation community.

CNTs are deposited radially on the surface of the primary fibers and they are also surrounded by matrix as investigated by Li et al. using SEM [19] (Figure 2). The fiber with CNT grafted radially can be represented schematically as in Figure 3. The interphase is commonly modeled as a homogeneous equivalent medium. Consequently, fuzzy fiber composites can be represented as a system of two concentric cylinders embedded within a matrix phase, resulting in a hierarchical, three-scale medium: the micro-scale (Figure 4c): CNTs in the matrix, the meso-scale (Figure 4b): fuzzy fiber in the matrix, and the macro-scale (Figure 4a): overall composite structure [13].

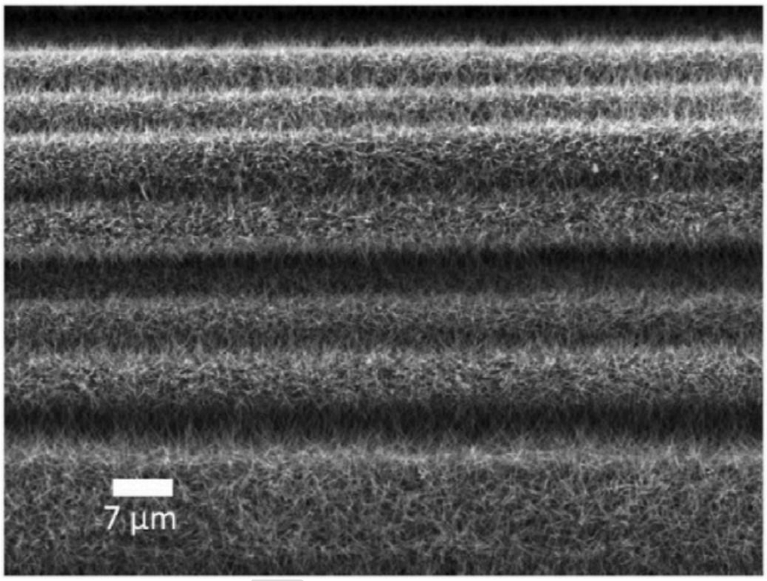

Figure 2: SEM image of fibers with densely-packed CNTs on their surfaces by Li et al. [19]. This figure is reproduced from the Composite Science and Technology, Vol. 117, titled Hierarchical carbon nanotube carbon fiber unidirectional composites with preserved tensile and interfacial properties by Richard Li, Noa Lachman, Peter Florin, H. Daniel Wagner, Brian L. Wardle, pp. 139-145, 2015, with permission from Elsevier.

The fuzzy fiber composite presents a complex, three-scale structure that requires a distinct approach at each scale to accurately capture the various interactions. Advanced multiscale homogenization techniques are crucial for accurately representing the behavior of such hierarchical materials. In the literature and in the field of micromechanics simulations, three primary approaches have been adopted to predict the effective properties of these

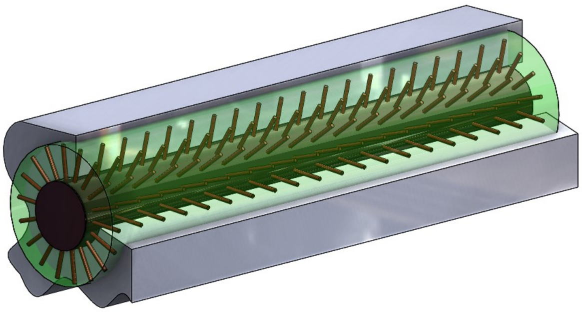

Figure 3: Schematic representation of a fuzzy fiber composite featuring carbon nanotubes (CNTs) grafted radially onto the fiber surface to improve the fiber-matrix interface.

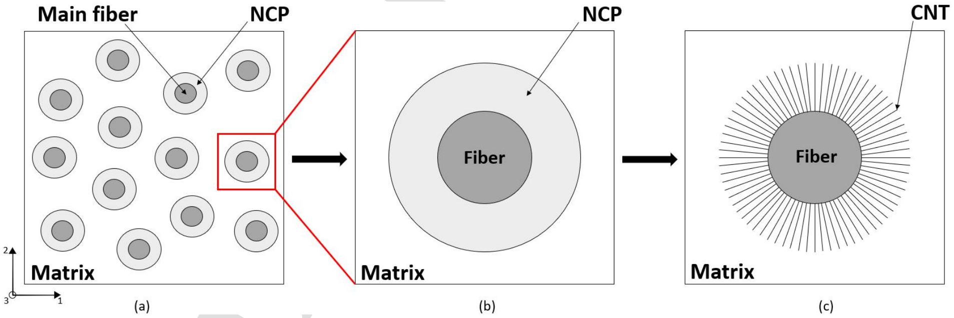

Figure 4: (a) Macroscopic scale of fuzzy fiber composites materials; (b) Mesoscale fuzzy fiber composite containing the main fiber, nanocomposite interphase, and matrix; (c) Microscale fuzzy fiber composite containing the main fiber, CNTs, and matrix phases.

composites. The first consists of the classical micromechanics method of the Mori-Tanaka model, which provides an effective estimation of composite properties. This model has been widely used to predict the initial yield strength and post-yield response in composite materials ([20], [21]). Classical micromechanics models use a uniform stress or strain distribution across each phase and consider interactions between adjacent reinforcements in an averaged way, providing an effective framework for understanding stress distribution and predicting damage evolution and plastic deformation within the composite microstructure. The second approach considers the composite cylinder assemblage (CCA) model that incorporates simplified geometric representations of the material's microstructure [22]. The third approach, based on periodic homogenization, provides detailed information about the effective response of the composite, as well as the distribution of stresses and strains across all scales essential for detecting potential damage prone areas [17].

The inclusion of a cylindrically orthotropic interphase layer introduces significant complications in the homogenization of composite materials. In standard Cartesian coordinates system, this interphase behaves as a functionally graded material, with varying properties with respect to the angular position and the radial distance. This complexity renders classical multiscale techniques inadequate for accurate modeling. Instead, advanced numerical homogenization methods are needed, as they are better suited to capture complex microstructural features and nonlinear material behavior. The rise in computational power has enabled more precise calculations of homogenized properties using full-field homogenization, solving the problem numerically via finite-elements ([23], [12], [24]), finite-volumes ([25], [26]) approaches and even Fast Fourier Transform technique (FFT, [27]). These methods have become dominant due to their ability to model complex unit cell structures containing randomly shaped and sized inclusions. They also accommodate various deformation mechanisms at the phase level, including plasticity [28] and viscoelastic-viscoplastic behavior [29]. For continuous fuzzy fiber reinforced composites, the effective properties have been determined using the method of cells and the finite-element method, as demonstrated by Kundalwal and Ray [30]. In addition to physics-based analytical and numerical techniques, machine learning-driven approaches have also shown promise in enhancing multiscale simulations of composite materials, offering new opportunities for predictive modeling [31].

The impact of CNT-reinforced interphases on the elastic and elastoplastic properties of composites has been well-studied in the literature through classical micromechanics models and periodic homogenization techniques ([14], [32], [33], [34] and [35]). However, much less research has been devoted to understanding how these interphases affect the elasto-visco-plastic response of materials. This study addresses the existing gap by formulating and applying an innovative hybrid hierarchical multiscale homogenization approach, specifically developed for the elasto-viscoplastic regime while incorporating the evolution of interfacial damage. It combines the composite cylinder assemblage (CCA) model with transformation field analysis (TFA), as developed by Chatzigeorgiou et al. [13], and then incorporates periodic homogenization theory. In a two-step homogenization process, the properties of the nanocomposite interphase are first computed and then applied to predict

---

the effective behavior of fuzzy fiber composites. Through this method, an intermediate equivalent fiber is created using CCA-based TFA, which effectively models both the fiber and CNT-reinforced interphase. This equivalent fiber then replaces the actual fiber-interphase system in traditional full-field homogenization, providing enhanced accuracy in predicting the composite's overall mechanical response.

The remainder of the paper is structured as follows: Section 2 presents the problem and microstructure under consideration, including a general description of the materials used for each phase and the concept of the equivalent fiber substitution. Section 3 illustrates the theoretical framework of transversely isotopic viscoplastic materials, the discret damage theory, the composite cylinders assemblage methodology and the transformation field analysis approach. In Section 4, numerical results are provided, including the properties of the nanocomposite and the fuzzy fiber composite. New numerical findings are presented to emphasize the strengths of the proposed theory and to compare it with the outcomes obtained from the equivalent fiber approach. In Section 5, a parametric study is conducted to investigate the influence of specific parameters on the stress-strain curves. These include ratios of certain areas within the fuzzy fiber, such as ϕ_1 and ϕ_2, as well as parameters related to the volume fraction, such as the matrix phase volume fraction. Section 6 draws key findings and outlines potential directions for future research.

2. Problem definition: Microstructure presentation of the Fuzzy Fiber composites

The purpose of this section is to describe the problem under investigation. Before detailing the different steps involved, it is necessary to provide some preliminary information regarding the microstructure being studied.

The hierarchical multiscale homogenization approach proposed in this study follows a three-step process:

1. In the first step, the nanocomposite (NCP) interphase, where the CNT-reinforced matrix material is present, is homogenized into an equivalent heterogeneous coating layer attached to the main fibers in a cylindrical coordinate system. This step yields the effective properties of the nanocomposite interphase.
2. In the second step, a coating element is introduced into the region between the nanocomposite (NCP) and the matrix to simulate discrete damage mechanisms, characterized by microvoid growth governed by an evolution law.
3. In the final step, a new equivalent fiber is developed to represent the fuzzy fiber. This equivalent fiber replaces the main fiber, the nanocomposite (NCP), and the coating, capturing the inelastic response of the coated main fiber. The modeling is performed using a cylindrical representative volume element, which is detailed further in the relevant section.

It is worth mentioning that, for the sake of simplicity, the CNTs are assumed to have uniform radii and lengths. The effects of CNT waviness

---

([13] and [15]) or irregular distribution patterns are not considered in this analysis.

In this work, we consider single-walled carbon nanotubes (SWCNTs). No specific choice of chirality (zigzag, armchair, or chiral) has been defined, and the CNTs have been represented as hollow cylinders made of graphene. While the atomistic-scale configuration of CNTs is not detailed in our manuscript, the assumption of hollow cylinder CNT aligns with our hierarchical multiscale modeling approach, which combines full-field and mean-field homogenization methods.

The microstructure of the composite demonstrates a uniform dispersion of CNTs throughout the matrix, forming a phase where the reinforcing effects of the CNTs synergistically interact with the matrix's properties, thereby enhancing the overall mechanical performance and electrical conductivity of the material. This precise distribution of CNTs within the matrix is critical for achieving the desired superior mechanical and conductive properties (Figure 5).

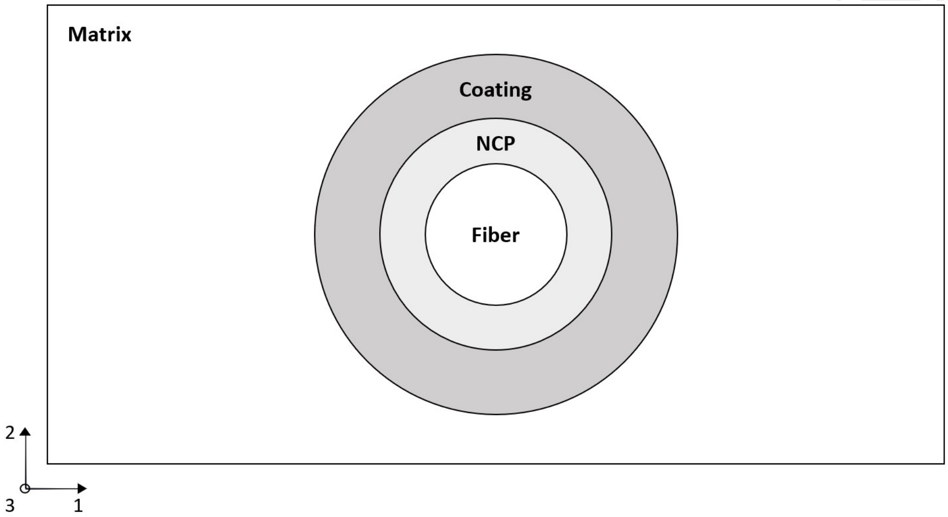

Figure 5: Schematic representation of the Fuzzy Fiber composite microstructure. The core fiber is surrounded by a nanocomposite (NCP) interphase reinforced with CNTs, followed by a coating layer, all embedded in the surrounding matrix. This microstructure serves as the basis for the multiscale homogenization approach.

To analyze the composite, the focus is given on the four primary materials involved (Figure 5):

- The **carbon fiber**, assumed to exhibit purely elastic behavior.
- The **nanocomposite (NCP)**, whose properties are identified using the periodic homogenization method. Its response is subsequently modeled using an appropriate phenomenological law. It is expected that the NCP behaves as a transversely isotropic viscoplastic medium, and the homogenization results of section 4.1 confirm it.
- The **coating**, at the nanocomposite (NCP)-matrix interface, where discrete damage phenomenon is introduced through microvoids growth

within an evolution law. This phase is modeled using a combination of a viscoplastic/damage law and the MoriTanaka scheme.

- The **matrix**, which consists of an isotropic viscoplastic material, is modeled using a viscoplastic phenomenological law.

To further streamline the analysis, the introduction of an equivalent fiber approach simplifies the model by substituting the three distinct phases (carbon fiber, NCP, and coating) with a single equivalent fiber. This hypothetical fiber is designed to replicate the overall mechanical properties and fields that arise from the contributions of the three phases.

3. Theoretical framework

This section discusses the main theoretical tools related with the current study. These include the description of constitutive laws that include viscoplasticity and discrete damage, as well as micromechanics concepts.

3.1. Transversely isotropic viscoplastic materials

Given the geometrical characteristics of the nanocomposite, it is expected that its overall behavior will be similar to a cylindrically transversely isotropic material with axis of symmetry parallel to the main fiber axis. This subsection discusses the constitutive law of a transversely isotropic viscoplastic medium [36].

For a typical isotropic material, the stress and strain tensors are decomposed into two components: a hydrostatic part and a deviatoric part.

$$\sigma_{ij} = \sigma_{ij}^{hyd} + \sigma_{ij}^{dev} = \sigma_{kk}\delta_{ij} + \sigma_{ij}^{dev}, \tag{1}$$

$$\epsilon_{ij} = \epsilon_{ij}^{hyd} + \epsilon_{ij}^{dev} = \epsilon_{kk}\delta_{ij} + \epsilon_{ij}^{dev}. \tag{2}$$

On a transversely isotropic material however, the stress and strain tensors are decomposed into a hydrostatic and two deviatoric components [37]. If the plane of symmetry is the 2-3, the stress and strain components in Voigt notation are expressed as

$$\boldsymbol{\sigma} = \boldsymbol{\sigma}^h + \boldsymbol{\sigma}^t + \boldsymbol{\sigma}^a, \tag{3}$$

$$\boldsymbol{\sigma}^h = \begin{bmatrix} \sigma_{11} \\ \frac{\sigma_{22}+\sigma_{33}}{2} \\ \frac{\sigma_{22}+\sigma_{33}}{2} \\ 0 \\ 0 \\ 0 \end{bmatrix}, \boldsymbol{\sigma}^t = \begin{bmatrix} 0 \\ \frac{\sigma_{22}-\sigma_{33}}{2} \\ \frac{\sigma_{33}-\sigma_{22}}{2} \\ 0 \\ 0 \\ \sigma_{23} \end{bmatrix}, \boldsymbol{\sigma}^a = \begin{bmatrix} 0 \\ 0 \\ 0 \\ \sigma_{12} \\ \sigma_{13} \\ 0 \end{bmatrix},$$

$$\boldsymbol{\epsilon} = \boldsymbol{\epsilon}^h + \boldsymbol{\epsilon}^t + \boldsymbol{\epsilon}^a, \tag{4}$$

$$\boldsymbol{\epsilon}^h = \begin{bmatrix} \epsilon_{11} \\ \frac{\epsilon_{22}+\epsilon_{33}}{2} \\ \frac{\epsilon_{22}+\epsilon_{33}}{2} \\ 0 \\ 0 \\ 0 \end{bmatrix}, \boldsymbol{\epsilon}^t = \begin{bmatrix} 0 \\ \frac{\epsilon_{22}-\epsilon_{33}}{2} \\ \frac{\epsilon_{33}-\epsilon_{22}}{2} \\ 0 \\ 0 \\ 2\epsilon_{23} \end{bmatrix}, \boldsymbol{\epsilon}^a = \begin{bmatrix} 0 \\ 0 \\ 0 \\ 2\epsilon_{12} \\ 2\epsilon_{13} \\ 0 \end{bmatrix},$$

The stiffness matrix **L** for a transversely isotropic material with axis of symmetry parallel to the direction 3, relates the stresses to the strains as follows

$$\mathbf{L} = \begin{bmatrix} n & l & l & 0 & 0 & 0 \\ l & K^{tr}+\mu^{tr} & K^{tr}-\mu^{tr} & 0 & 0 & 0 \\ l & K^{tr}-\mu^{tr} & K^{tr}+\mu^{tr} & 0 & 0 & 0 \\ 0 & 0 & 0 & \mu^{ax} & 0 & 0 \\ 0 & 0 & 0 & 0 & \mu^{ax} & 0 \\ 0 & 0 & 0 & 0 & 0 & \mu^{tr} \end{bmatrix}, \tag{5}$$

In the above equation, K^{tr} denotes the plane strain bulk modulus, μ^{tr} denotes the transverse shear modulus, μ^{ax} denotes the axial shear modulus, n is the modulus related to the axial tensile loading, and l reflects the coupling between the axial tension and transverse tension loadings.

In addition, for a viscoplastic material, the stress-strain relation is expressed as

$$\boldsymbol{\sigma} = \mathbf{L} : (\boldsymbol{\epsilon} - \boldsymbol{\epsilon}_p), \tag{6}$$

Considering $\mathbf{L} = \mathbf{L}^h + \mathbf{L}^t + \mathbf{L}^a$ with

$$\mathbf{L}^h = \begin{bmatrix} n & l & l & 0 & 0 & 0 \\ l & K^{tr} & K^{tr} & 0 & 0 & 0 \\ l & K^{tr} & K^{tr} & 0 & 0 & 0 \\ 0 & 0 & 0 & 0 & 0 & 0 \\ 0 & 0 & 0 & 0 & 0 & 0 \\ 0 & 0 & 0 & 0 & 0 & 0 \end{bmatrix},$$

$$\mathbf{L}^t = \begin{bmatrix} 0 & 0 & 0 & 0 & 0 & 0 \\ 0 & \mu^{tr} & -\mu^{tr} & 0 & 0 & 0 \\ 0 & -\mu^{tr} & \mu^{tr} & 0 & 0 & 0 \\ 0 & 0 & 0 & 0 & 0 & 0 \\ 0 & 0 & 0 & 0 & 0 & 0 \\ 0 & 0 & 0 & 0 & 0 & \mu^{tr} \end{bmatrix},$$

$$\mathbf{L}^a = \begin{bmatrix} 0 & 0 & 0 & 0 & 0 & 0 \\ 0 & 0 & 0 & 0 & 0 & 0 \\ 0 & 0 & 0 & 0 & 0 & 0 \\ 0 & 0 & 0 & \mu^{ax} & 0 & 0 \\ 0 & 0 & 0 & 0 & \mu^{ax} & 0 \\ 0 & 0 & 0 & 0 & 0 & 0 \end{bmatrix},$$

and that viscoplasticity appears only under deviatoric conditions, the constitutive law can be decomposed in the terms

$$\boldsymbol{\sigma}^h = \mathbf{L}^h : \boldsymbol{\epsilon}^h, \qquad \boldsymbol{\sigma}^t = \mathbf{L}^t : [\boldsymbol{\epsilon}^t - \boldsymbol{\epsilon}^{tp}], \qquad \boldsymbol{\sigma}^a = \mathbf{L}^a : [\boldsymbol{\epsilon}^a - \boldsymbol{\epsilon}^{ap}]. \quad (7)$$

Since the hydrostatic part does not atribute to the nonlinear behavior, only five viscoplastic strain components appear. These follow evolution laws of the form

$$\dot{\epsilon}_{22}^{tp} = -\dot{\epsilon}_{33}^{tp} = \frac{\sigma_{22}^t}{2s^t}\dot{p}^t, \quad 2\dot{\epsilon}_{23}^{tp} = \frac{\sigma_{23}^t}{s^t}\dot{p}^t, \quad (8)$$

$$2\dot{\epsilon}_{12}^{ap} = \frac{\sigma_{12}^a}{s^a}\dot{p}^a, \quad 2\dot{\epsilon}_{13}^{ap} = \frac{\sigma_{13}^a}{s^a}\dot{p}^a. \quad (9)$$

The form of the evolution laws imply that the axial and the shear deviatoric inelastic responses are driven by two different scalars, p^a and p^t. The evolution of these scalars are dictated by two separate, given by the equations 10 and 11

$$\phi_{VP}^t = \sqrt{\frac{1}{2}\sigma_{ij}^t\sigma_{ij}^t} - [Y^t + Q_1^t p^t + Q_2^t(1 - e^{-b^t p^t})] - K_a^t \dot{p}^{t\,\frac{1}{N_a^t}} \leq 0, \quad (10)$$

$$\phi_{VP}^a = \sqrt{\frac{1}{2}\sigma_{ij}^a\sigma_{ij}^a} - [Y^a + Q_1^a p^a + Q_2^a(1 - e^{-b^a p^a})] - K_a^a \dot{p}^{a\,\frac{1}{N_a^a}} \leq 0, \quad (11)$$

where the subscripts t and a indicate transverse and axial deviatoric terms respectively.

The material properties of this constitutive law are identified from a periodic homogenization analysis performed at the NCP. The details of this analysis are provided in later sections.

3.2. Discrete damage theory

In this study, a special type of coating is employed to account for the damage occurring between the actual matrix and the NCP due to large stress mismatches. This damage is discrete and is represented through the formation of microvoids and microcracks (Figure 6). As microvoids and microcracks emerge, they serve as early indicators of material degradation, reflecting the progressive weakening that eventually leads to failure.

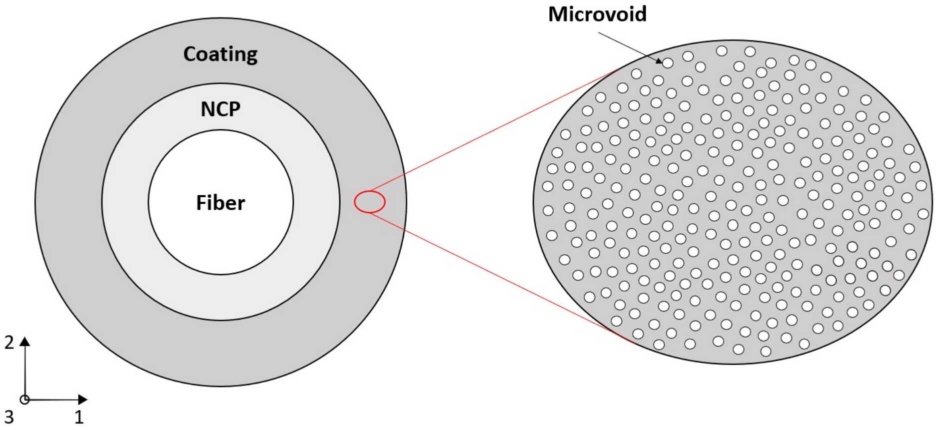

Figure 6: Schematic representation of the composite microstructure highlighting the damage mechanisms at the nanocomposite (NCP)-matrix interface. A coating made of a viscoplastic media coupled with discrete damage material (VPD) is employed to account for the stress-induced damage, forming discrete microvoids and microcracks, which signal material degradation and eventual failure.

The coating is composed of a viscoplastic media coupled with discrete damage material (VPD), in which damage is treated as a discrete phenomenon. The damage evolution is governed by a set of parameters, including the total strain $\boldsymbol{\epsilon}$, the viscoplastic strain $\boldsymbol{\epsilon}_p$, the effective viscoplastic strain p, and the microvoid density γ_c. These variables interact to define the constitutive behavior of the coating.

The constitutive law captures the complex interplay between strain, viscoplasticity, and damage evolution, providing insight into the material's response to the loading conditions and its accumulation prior to the failure. The stress-strain relationship of the coating takes the form

$$\boldsymbol{\sigma} \;=\; \boldsymbol{C}^{*} : (\boldsymbol{\epsilon} - \boldsymbol{\epsilon}_{p}), \tag{12}$$

Where

$$\boldsymbol{C}^{*} \;=\; \boldsymbol{C} - \boldsymbol{D}(\gamma_c), \tag{13}$$

$\boldsymbol{C}$ is the isotropic elastic fourth order tensor and $\boldsymbol{D}(\gamma_c)$ is the damage related fourth order tensor. Since the coating (VPD) is modeled as a zone where damage occurs in the form of spherical microvoids (Figure 6), the variable γ_c, represents the density of microvoids, is equivalent to the void volume fraction, and is initially zero.

In this model, the damage affects primarily the elastic response of the material. In addition, the damage evolves through the voids density accumulation, which is illustrated by the equation (20). This approach ensures that the damage evolution remains implicitly coupled with the viscoplastic behavior, through σ^{VM} which governs the evolution of γ_c allowing for a more accurate representation of the material's degradation.

$\boldsymbol{C}^{*}$ in equation (13) represents the properties of the damaged region, which was initially an isotropic viscoplastic matrix. However, spherical microcracks have been introduced. The C^{*} of the two-phase damaged composite (matrix + spherical voids) has been obtained using the MoriTanaka scheme, as given in equations (14), (15), and (16) accounting for the variable γ_c as the void volume fraction.

Using the Hill's notation, $\boldsymbol{C}^{*}$ can be written as an isotropic elastic material and can be expressed as

$$\begin{aligned} \boldsymbol{C}^* &= \boldsymbol{C} - \boldsymbol{D}(\gamma_c) = (3K^*, 2\mu^*), \qquad (14)\\ K^* &= K[1-\gamma_c]\frac{4\mu}{3K\gamma_c + 4\mu}, \qquad (15)\\ \mu^* &= \mu[1-\gamma_c]\frac{9K+8\mu}{3K[3+2\gamma_c]+4\mu[2+3\gamma_c]}. \qquad (16) \end{aligned}$$

Where K and μ are the bulk and shear moduli respectively.

The evolution laws for the internal viscoplastic variables and activation criteria for the damage are

$$\dot{\epsilon}_p = \dot{p} \wedge_p (\sigma), \qquad (17)$$

$$\wedge_p(\sigma) = \frac{3\sigma'}{2\sigma^{VM}}, \quad \sigma' = \sigma - \frac{1}{3}[tr(\sigma)]I, \quad \sigma^{VM} = \sqrt{\frac{3}{2}\sigma' : \sigma'}, \qquad (18)$$

$$\phi_p = \frac{1}{K_a^{N_a}} \langle \sigma^{VM} - R(p) - R_0 \rangle_+^{N_a} - \dot{p} = 0, \qquad \dot{p} \geq 0, \qquad (19)$$

$$\gamma_c = \gamma_{max}\left[1 - \exp\left(-\left(\frac{\langle sup(\sigma^{VM} - \sigma_a)\rangle_+}{\sigma_c}\right)^k\right)\right]. \qquad (20)$$

Where γ_{max}, σ_a, σ_c and k are known damage related constants.

Since the coating region is of similar material with the matrix, the matrix phase is expressed also by a similar constitutive law excluding the damage mechanism.

3.3. Composite cylinder assemblage approach (CCA)

For the composite cylinder method, the RVE system to be addressed represents a dilute problem, comprising of a four layer composite, including: fiber with radius r_0, nanocomposite with external radius r_1, coating interphase with external radius r_2, and the matrix of infinite radius (Figure 7). The system's response is calculated through the Eshelby inhomogeneity problem, with a three-phase medium (fiber, NCP, and coating) embedded within an infinite matrix subjected to the boundary condition $\boldsymbol{U} = \epsilon_0 \cdot \boldsymbol{x}$, where ϵ_0 prescribed strain applied at the mesoscale. The dilute concentration tensors are then determined using the Composite Cylinder Assemblage (CCA) method. This approach can be further generalized to cases involving more than four layers.

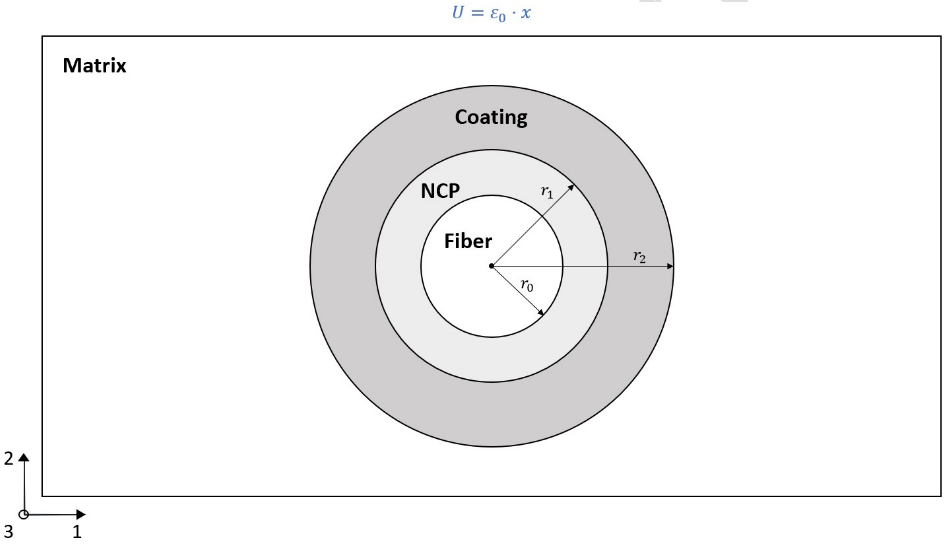

Figure 7: Eshelby dilute inhomogeneity problem where the fiber with radius r_0, the nanocomposite NCP with external radius r_1 and the coating interphase with external radius r_2 are embedded in the infinite matrix subjected to the boundary condition $\boldsymbol{U} = \epsilon_0 \cdot \boldsymbol{x}$.

The theoretical formulation of the homogenization process is carried out using two orthogonal coordinate systems: cylindrical coordinates (z, r, θ) and Cartesian coordinates (x_1, x_2, x_3). The transformation relationship between these two coordinate systems is expressed as follows

$$x_1 = r\cos\theta \qquad x_2 = r\sin\theta \qquad x_3 = z. \tag{21}$$

Due to the geometrical characteristics of the inhomogeneities, the theoretical formulation of the homogenization process is carried out using the cylindrical coordinates, using a system of concentric cylinders for the fiber, the nanocomposite and the coating. In the cylindrical coordinate system, the equilibrium equations for each phase are written as

$$\frac{\partial \sigma_{rr}}{\partial r} + \frac{1}{r}\frac{\partial \sigma_{r\theta}}{\partial \theta} + \frac{\partial \sigma_{rz}}{\partial z} + \frac{\sigma_{rr} - \sigma_{\theta\theta}}{r} = 0, \tag{22}$$

$$\frac{\partial \sigma_{r\theta}}{\partial r} + \frac{1}{r}\frac{\partial \sigma_{\theta\theta}}{\partial \theta} + \frac{\partial \sigma_{\theta z}}{\partial z} + \frac{2\sigma_{r\theta}}{r} = 0, \tag{23}$$

$$\frac{\partial \sigma_{rz}}{\partial r} + \frac{1}{r}\frac{\partial \sigma_{\theta z}}{\partial \theta} + \frac{\partial \sigma_{zz}}{\partial z} + \frac{\sigma_{rz}}{r} = 0. \tag{24}$$

Considering small deformation gradients, the strain field components, at each phase, are connected with the displacements through the following expressions

$$\boldsymbol{\epsilon} = \begin{bmatrix} \epsilon_{rr} \\ \epsilon_{\theta\theta} \\ \epsilon_{zz} \\ 2\epsilon_{r\theta} \\ 2\epsilon_{rz} \\ 2\epsilon_{\theta z} \end{bmatrix} = \begin{bmatrix} \frac{\partial u_r}{\partial r} \\ \frac{1}{r}\frac{\partial u_\theta}{\partial \theta} + \frac{u_r}{r} \\ \frac{\partial u_z}{\partial z} \\ \frac{\partial u_\theta}{\partial r} + \frac{1}{r}\frac{\partial u_r}{\partial \theta} - \frac{u_\theta}{r} \\ \frac{\partial u_z}{\partial r} + \frac{\partial u_r}{\partial z} \\ \frac{1}{r}\frac{\partial u_z}{\partial \theta} + \frac{\partial u_\theta}{\partial r} \end{bmatrix}. \tag{25}$$

Concerning the analytical homogenization strategy, average fields per phase are required to be computed. Considering the phase q, which has inner radius r_a, outer radius r_b and length $2L$, its average total fields in Cartesian coordinates are given by the expressions

$$< \boldsymbol{\epsilon} > \; = \; \frac{1}{2L\pi[r_b^2 - r_a^2]} \int_{L}^{-L} \int_{2\pi}^{0} \int_{r_b}^{r_a} \boldsymbol{Q}_{\sigma}^{T}.\boldsymbol{\epsilon}^{cyl} r dr d\theta dz, \qquad (26)$$

$$< \boldsymbol{\sigma} > \; = \; \frac{1}{2L\pi[r_b^2 - r_a^2]} \int_{L}^{-L} \int_{2\pi}^{0} \int_{r_b}^{r_a} \boldsymbol{Q}_{\epsilon}^{T}.\boldsymbol{\sigma}^{cyl} r dr d\theta dz. \qquad (27)$$

The stress rotation matrix $\boldsymbol{Q}_{\sigma}$ and the strain rotation matrix $\boldsymbol{Q}_{\epsilon}$ are given in Appendix A.

The integration of the constitutive law from subsection 3.1 into the composite cylinder assemblage (CCA) approach is accomplished as follows: all equations outlined in subsection 3.1 are represented in cylindrical coordinates to describe the material response.

The inelastic strains of the phases are integrated using the Transformation Field Analysis theory (discussed in the next subsection).

A unidirectional long fiber composite behaves as a transversely isotropic material. The aim of the composite cylinder assemblage approach is to provide five independent parameters of the composite material. These parameters are computed by solving the boundary value problems of table 1.

	Axial shear conditions	**Transverse shear conditions**	**Transverse normal conditions**	**Axial normal conditions**
Displacement boundary conditions	$u_{z(ext)} = \beta r_m \cos\theta$ 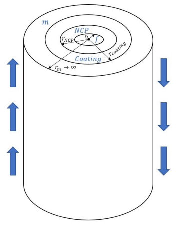 	$u_{\theta(ext)} = \beta r_m \cos 2\theta$ $u_{r(ext)} = \beta r_m \sin 2\theta$ 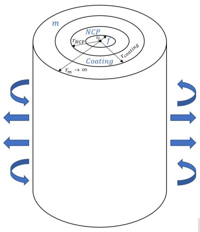 	$u_{r(ext)} = \beta r_m$ 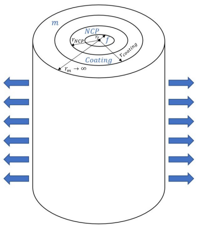 	$u_{z(ext)} = \pm\beta L$ 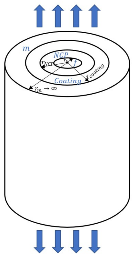

Table 1: Displacement boundary conditions for the composite cylinder assemblage approach to determine the key parameters of a transversely isotropic material in different loading conditions: axial shear, transverse shear, transverse normal, and axial normal conditions.

308 The obtained effective properties are the transverse (or inplane) bulk modulus K^{tr}, the axial shear modulus μ^{ax}, the axial Young modulus E^{ax}, the axial Poisson ratio ν^{ax}, and the transverse shear modulus μ^{tr}. With these

five parameters, we can identify the complete elasticity tensor $\boldsymbol{L}$.

$$\boldsymbol{L} = \begin{bmatrix} K^{tr}+\mu^{tr} & K^{tr}-\mu^{tr} & l & 0 & 0 & 0 \\ K^{tr}-\mu^{tr} & K^{tr}+\mu^{tr} & l & 0 & 0 & 0 \\ l & l & n & 0 & 0 & 0 \\ 0 & 0 & 0 & \mu^{tr} & 0 & 0 \\ 0 & 0 & 0 & 0 & \mu^{ax} & 0 \\ 0 & 0 & 0 & 0 & 0 & \mu^{ax} \end{bmatrix}.$$

In transversely isotropic phases (where the axis of symmetry is the zdirection), the stress and strain tensors are connected through the relation

$$\begin{bmatrix} \sigma_{rr} \\ \sigma_{\theta\theta} \\ \sigma_{zz} \\ \sigma_{r\theta} \\ \sigma_{rz} \\ \sigma_{\theta z} \end{bmatrix} = \boldsymbol{L}. \begin{bmatrix} \epsilon_{rr} \\ \epsilon_{\theta\theta} \\ \epsilon_{zz} \\ 2\epsilon_{r\theta} \\ 2\epsilon_{rz} \\ 2\epsilon_{\theta z} \end{bmatrix}.$$

The interface between the phase q ($q = f, ncp, coating$) and the phase s

---

$(s = ncp, coating, m)$ should satisfy the following continuity conditions at r_m $(m = 0, 1, 2, 3)$:

$$
\begin{aligned}
u_r^{(q)}(r_m, \theta, z) &= u_r^{(s)}(r_m, \theta, z), \\
u_\theta^{(q)}(r_m, \theta, z) &= u_\theta^{(s)}(r_m, \theta, z), \\
u_z^{(q)}(r_m, \theta, z) &= u_z^{(s)}(r_m, \theta, z), \\
\sigma_{rr}^{(q)}(r_m, \theta, z) &= \sigma_{rr}^{(s)}(r_m, \theta, z), \\
\sigma_{r\theta}^{(q)}(r_m, \theta, z) &= \sigma_{r\theta}^{(s)}(r_m, \theta, z), \\
\sigma_{rz}^{(q)}(r_m, \theta, z) &= \sigma_{rz}^{(s)}(r_m, \theta, z). \qquad (28)
\end{aligned}
$$

3.4. Transformation field analysis: transversely isotropic material case

The Transformation Field Analysis (TFA) method is employed to account for inelastic mechanisms in the equivalent fiber obtained by the procedure described in subsection 3.3. This approach connects local deformations and stresses in the various phases of the composite material to a homogenized response at the macroscopic level.

Each phase experiences its own inelastic stress, and the goal is to analyze this behavior under various conditions (Figure 8) and determine the average strains and stresses at each phase of the equivalent fiber.

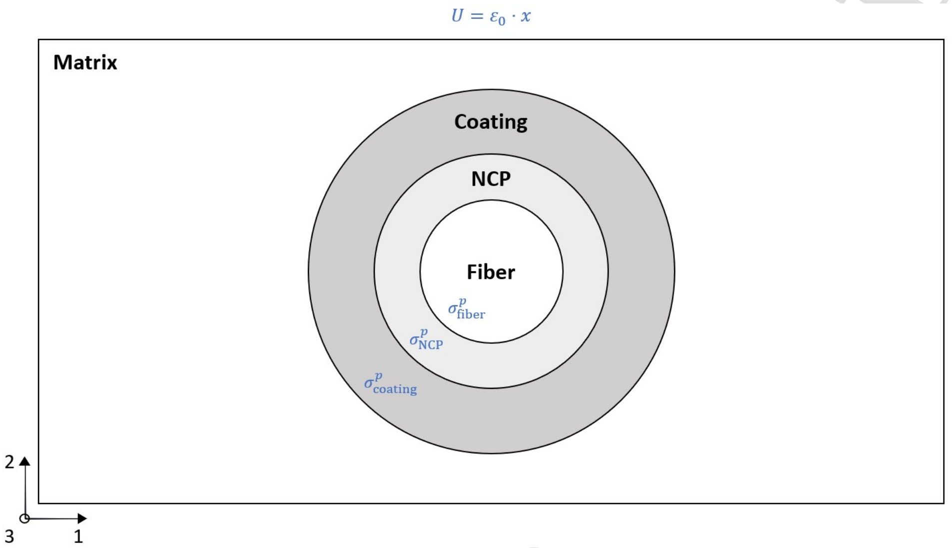

Figure 8: Schematic representation of the eshelby inhomogeneity problem. The figure illustrates the different phases of the equivalent fiber (fiber, NCP phase, coating, and infinite matrix) and their respective inelastic stresses (σ^p_f, σ^p_{NCP}, $\sigma^p_{\text{coating}}$).

The average strain ϵ_i and stress σ_i in each phase i are expressed as

$$\begin{aligned}
\boldsymbol{\epsilon}_i &= \boldsymbol{T}_i : \boldsymbol{\epsilon}_0 + \hat{\boldsymbol{\epsilon}}^p_i, \\
\hat{\boldsymbol{\epsilon}}^p_i &= \boldsymbol{T}^p_{h,i} : \boldsymbol{\sigma}^p_h + \sum_{j=1}^{N} \boldsymbol{T}^p_{j,i} : \boldsymbol{\sigma}^p_j, \quad i = h, 1, 2, \ldots, N.
\end{aligned}$$

$$\begin{aligned}
\boldsymbol{\sigma}_i &= \boldsymbol{H}_i : \boldsymbol{\epsilon}_0 + \hat{\boldsymbol{\sigma}}^p_i, \\
\hat{\boldsymbol{\sigma}}^p_i &= \boldsymbol{H}^p_{h,i} : \boldsymbol{\sigma}^p_h + \sum_{j=1}^{N} \boldsymbol{H}^p_{j,i} : \boldsymbol{\sigma}^p_j, \quad i = h, 1, 2, \ldots, N.
\end{aligned}$$

Where σ^p_j prescribed the average inelastic stress per phase, ϵ_0 stands for the average strain in the matrix, $\boldsymbol{T}$ and $\boldsymbol{H}$ are the dilute concentration tensors for strain-type and stress-type, respectively, while T^p and H^p are the inelastic tensors for strain-type and stress-type, respectively. Herein, a constant inelastic stress within each phase is assumed.

For the equivalent fiber, the equivalent strain is the average of all strains weighted by the relative volume fraction.

$$\begin{aligned}
\boldsymbol{\epsilon}_{eq} &= \phi_{fiber}.\boldsymbol{\epsilon}_{fiber} + \phi_{NCP}.\boldsymbol{\epsilon}_{NCP} + \phi_{coating}.\boldsymbol{\epsilon}_{coating}, \\
\boldsymbol{\sigma}_{eq} &= \phi_{fiber}.\boldsymbol{\sigma}_{fiber} + \phi_{NCP}.\boldsymbol{\sigma}_{NCP} + \phi_{coating}.\boldsymbol{\sigma}_{coating}.
\end{aligned}$$

where ϕ_i is the volume fraction of each phase in the equivalent inhomogeneity.

With this representation, the equivalent fiber is given by

$$\begin{aligned}
\boldsymbol{\epsilon}_{eq} &= \boldsymbol{T}_{eq} : \boldsymbol{\epsilon}_0 + \hat{\boldsymbol{\epsilon}}^p_{eq}, \\
\boldsymbol{T}_{eq} &= \phi_{fiber} \cdot \boldsymbol{T}_{fiber} + \phi_{NCP} \cdot \boldsymbol{T}_{NCP} + \phi_{coating} \cdot \boldsymbol{T}_{coating}, \\
\hat{\boldsymbol{\epsilon}}^p_{eq} &= \phi_{fiber} \cdot \hat{\boldsymbol{\epsilon}}^p_{fiber} + \phi_{NCP} \cdot \hat{\boldsymbol{\epsilon}}^p_{NCP} + \phi_{coating} \cdot \hat{\boldsymbol{\epsilon}}^p_{coating}.
\end{aligned}$$

and

$$\begin{aligned}
\boldsymbol{\sigma}_{eq} &= \boldsymbol{H}_{eq} : \boldsymbol{\epsilon}_0 + \hat{\boldsymbol{\sigma}}^p_{eq}, \\
\boldsymbol{H}_{eq} &= \phi_{fiber} \cdot \boldsymbol{H}_{fiber} + \phi_{NCP} \cdot \boldsymbol{H}_{NCP} + \phi_{coating} \cdot \boldsymbol{H}_{coating}, \\
\hat{\boldsymbol{\sigma}}^p_{eq} &= \phi_{fiber} \cdot \hat{\boldsymbol{\sigma}}^p_{fiber} + \phi_{NCP} \cdot \hat{\boldsymbol{\sigma}}^p_{NCP} + \phi_{coating} \cdot \hat{\boldsymbol{\sigma}}^p_{coating}.
\end{aligned}$$

The behavior of the equivalent fiber and the related mesoscopic quantities are now established, the next step is to perform the linear homogenization of the composite. To this end, all previously obtained results must be transformed from the cylindrical coordinate system to the Cartesian coordinate system. This transition is an integral part of the full-field homogenization process, which accounts for the equivalent fiber. Following this, the average values derived from the homogenization step are transformed into Cartesian coordinates using the specified equations.

4. Numerical results

In this section, numerical examples of a fuzzy fiber composite with multiple phases are presented. The scope is to examine the properties of the fuzzy fiber composite resulting from the addition of a coating around the nanocomposite. As for conventional composites, the interface between the polymer matrix and the nanocomposites governs the overall response of the composite due to the various complex load-transfer occuring in this region. Adding a coating layer around the nanocomposite aims to capture more accurately these interactions. While the nanocomposite enhances mechanical properties such as strength and stiffness, the coating layer introduces several damage mechanisms.

As mentioned before, the fuzzy fiber composite studied herein consist of four material phases (Figure 8). The matrix is assumed to be represented by the viscoplasticity of isotropic polymer. The main fiber is made of isotropic glass which is taken to have a purely elastic behavior during the entire deformation history. The carbon nanotube is made of graphene. The elastic properties for all these materials taken from [2] are listed in the table 2.

	Graphene	**Glass fiber**
E (GPa)	1100	72
ν	0.14	0.2

Table 2: Elastic properties of the graphene and the glass fiber (Chatzigeorgiou et al., [2]).

The overall properties of fuzzy fiber composites are strongly influenced by key geometrical parameters, such as the thickness of the CNT interface and the radii of the main fibers, as well as the volume content of the CNTs, which are hollow microfibers made of graphene.

In this study, the CNTs are defined with an inner radius of $0.51nm$ and an outer radius of $0.85nm$ (Chatzigeorgiou et al., [2]). The radius of the glass fiber is $2.5\mu m$. The CNT length, which also represents the thickness of the nanocomposite coating layer, is set to $2\mu m$ and the coating thickness is $1\mu m$. The dimensions of the main fiber and the nanocomposite interphase are held constant, with the volume fraction of CNTs within the nanocomposite interphase set at 10%. The volume fraction of the composite fiber (NCP + main fiber) in the entire fuzzy fiber composite system is 30%.

It is worth mentioning that the number of CNTs grown around the fiber is not a parameter used in this work. Instead, the microscopic calculations are based on a fixed volume fraction of 10% of CNTs inside the NCP. For further details on the limitation in the maximum number of CNTs that can be radially grown around a fiber due to the van der Waals interactions between adjacent CNTs, the interested reader can refer to the work of Kundalwal and Ray [38].

4.1. Microscale homogenization: effective response of the nanocomposite

The properties of the NCP are determined using the classical periodic homogenization method. The nanocomposite considered in this section consists of three distinct material phases (Figure 9): the matrix, modeled as a viscoplastic isotropic material; the central cylindrical part, representing the void region; and the carbon nanotubes, composed of graphene, which are also assumed to behave as isotropic materials.

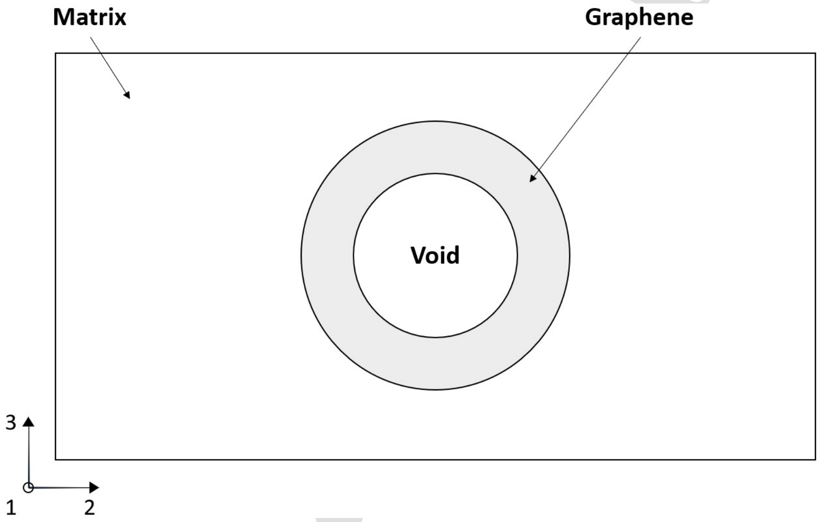

Figure 9: Schematic representation of the nanocomposite (NCP) analyzed in this study. The NCP consists of three distinct material phases: the matrix, modeled as a viscoplastic isotropic material; the graphene-based carbon nanotubes (CNTs), modeled as isotropic materials; and the void, made by rolling up the graphene into a cylinder.

Herein, the elastic-viscoplastic model of the matrix used in the present work is a typical one with isotropic hardening and Norton's viscoplastic law [39]. Under monotonic and uniaxial conditions, the equivalent von Mises stress equals the axial stress σ, and the axial plastic strain ϵ_p is equal to the equivalent plastic strain p. The hardening law is given by:

$$\sigma_p(p) \quad = \quad [Y + Q_1 p + Q_2(1 - e^{-bp})] + K_a \dot{p}^{\frac{1}{N_a}}, \tag{29}$$

where σ_p and p are the von Mises equivalent stress and the cumulative effective plastic strain,respectively. Y denotes the initial yield stress, Q_1 is a linear hardening modulus, Q_2 is a coefficient associated with the exponential hardening term, b represents the hardening rate, K_a is a coefficient related to the viscoplastic flow and N_a is the strain rate sensitivity exponent.

The parameters of this hardening law are identified through a reverse engineering method using experimental data available in the literature [40]. To maintain the validity of the small deformation assumption, the analysis is limited to strain levels below 10%. Figure 10 shows the nominal stress-strain curves in compressive loading at room temperature at the nominal strain rates of $10^{-5}/s$, $10^{-3}/s$ and $10^{-1}/s$. The Figure 10 shows the experimental graphs compared to the simulation results computed on the basis of the material parameters identification.

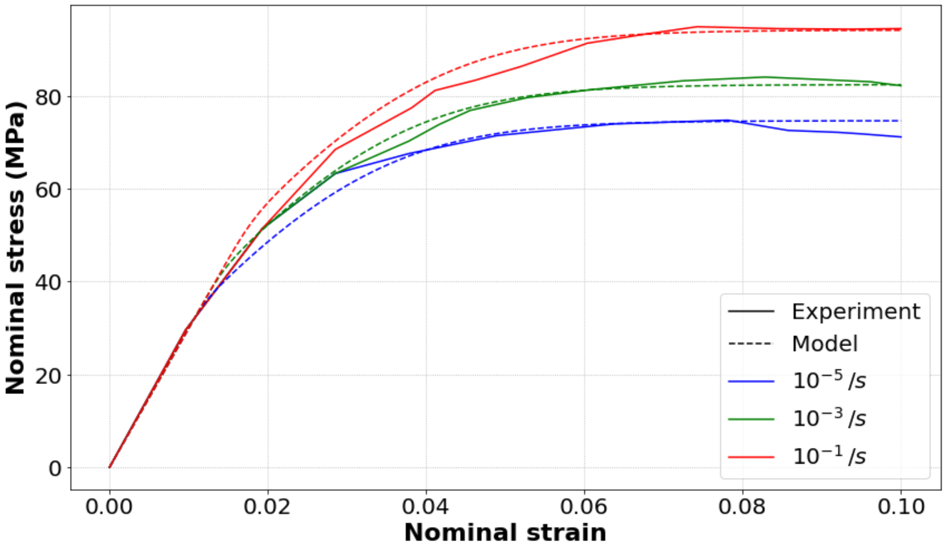

Figure 10: Nominal stressstrain responses of the pure matrix under compressive test performed at room temperature conditions at $T = 25\,^{\circ}\mathrm{C}$, evaluated at nominal strain rates of $10^{-5}\,\mathrm{s}^{-1}$, $10^{-3}\,\mathrm{s}^{-1}$, and $10^{-1}\,\mathrm{s}^{-1}$.

407 The identified parameters are listed in the table 3. Their values are
408 obtained by minimizing a cost function of the form:

$$\lambda = \arg\min F(\lambda), \tag{30}$$

$$F(\lambda) = \sum_{i=1}^{N} \frac{(\sigma_i^{\text{numerical}} - \sigma_i^{\text{experimental}})^2}{2}. \tag{31}$$

Property of the matrix	**Value**
E (GPa)	2.99
ν	0.33
Y (MPa)	21.7
Q_1 (MPa)	0
Q_2 (MPa)	37.7
K_a (MPa.s$^{1/N_a}$)	42.8
N_a	11.2
b	106.6

Table 3: Elastic and viscoplastic properties of the matrix identified from experimental curves of Figure 10 using the least squares method combined with trust region reflective algorithm (trf) [41].

This constitutive law is implemented in numerical calculations through a Fortran User Material (UMAT) subroutine.

At the next step, periodic homogenization is applied at the RVE shown in Figure 11. The elements are tetrahedral and of the C3D10 type. Axial loading along the 1st axis and shear loading conditions along the 2-3 and 1-3 planes are considered. It is noted that prior to the computations, a mesh sensitivity analysis had been conducted for different mesh sizes confirming the spatial convergence of the predicted macroscopic response.

The resulting data, depicted in the form of curves, provide insight into the NCP's response under the above three loading conditions (figures 12, 13 and 14).

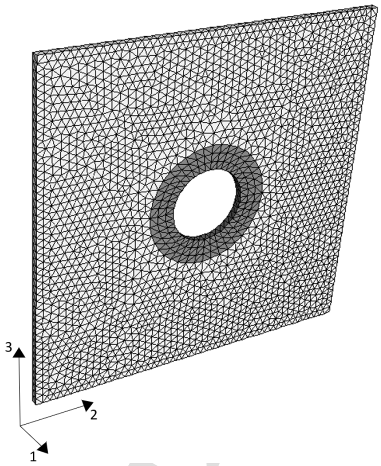

Figure 11: Repeating unit cell of the nanocomposite (NCP), comprising of graphene, void, and matrix phases. The Representative Volume Element (RVE) is discretized using tetrahedral elements of the C3D10 type and is subjected to periodic boundary conditions (PBC).

It is worth mentioning that the choice of the square unit cell shown in Figure 11, is motivated by the observation that the hexagonal unit cell fails to preserve transverse isotropy within the nonlinear regime of the overall stressstrain response [42]. While in tetragonal arrangement the transversely isotropic relationships between the transverse Youngs moduli and the transverse shear modulus are no longer applicable. It still yields isotropic response under transverse tensile loading in the plane perpendicular to the fiber direction. In contrast, the hexagonal arrangement generates different stressstrain responses under transverse tensile loading at the directions 2 and 3.

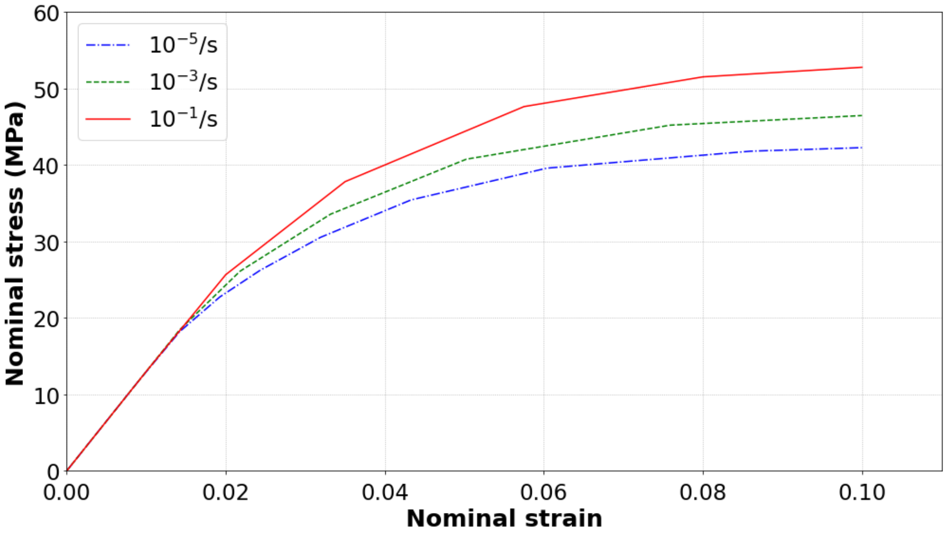

Figure 12: Nominal stress-strain response of NCP in shear testing along plane 2-3 at strain rates of 10^{-5}, 10^{-3}, and 10^{-1} s^{-1}.

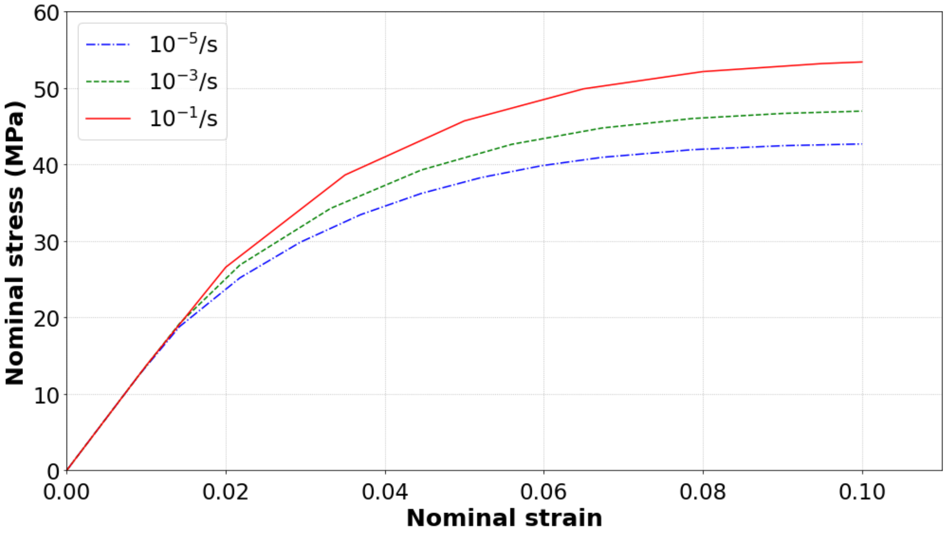

Figure 13: Nominal stress-strain response of NCP in shear testing along plane 1-3 at strain rates of 10^{-5}, 10^{-3}, and 10^{-1} s^{-1}.

Given the overall stress-strain curves depicted in figures 12 and 13, the overall NCP behaves as a transversely isotropic viscoplastic material.This confirms the theoretical background considering the transversely isotropic viscoplastic material described in subsection 3.1.

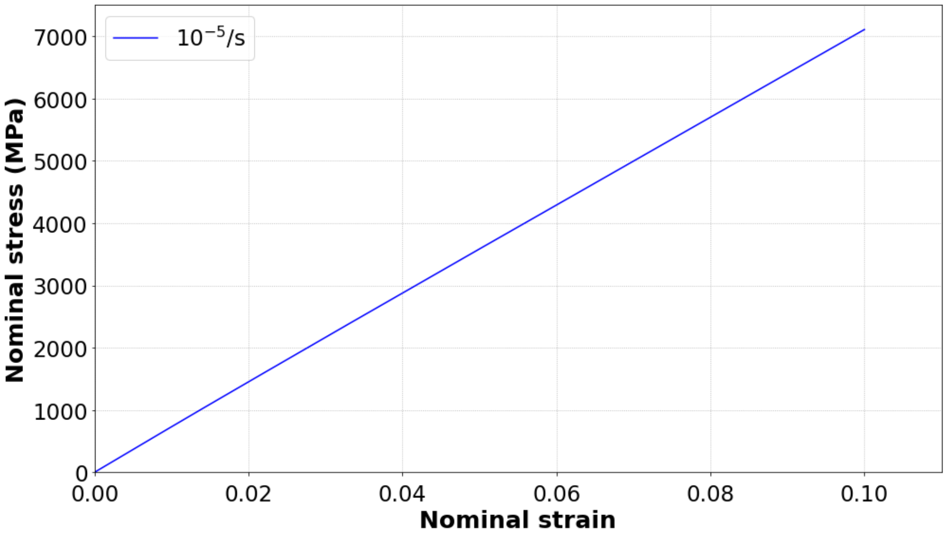

Figure 14: Nominal stress-strain response of NCP in uniaxial testing along direction 3 at strain rates of 10^{-5}, 10^{-3}, and 10^{-1} s^{-1}.

As expected, Figure 14 clearly demonstrates the absence of plasticity in direction 3. This observation motivated the incorporation of a coating phase with discrete damage around the NCP.

The figures 15 and 16 illustrate the results of the shear loading conditions at planes 2-3 and 1-3 on the RVE of NCP under loading rates of 10^{-5}, 10^{-3} and 10^{-1} (1/s). When the loading rate decreases, the effect of stress concentration around the void decrease progressively, indicating higher concentrations.

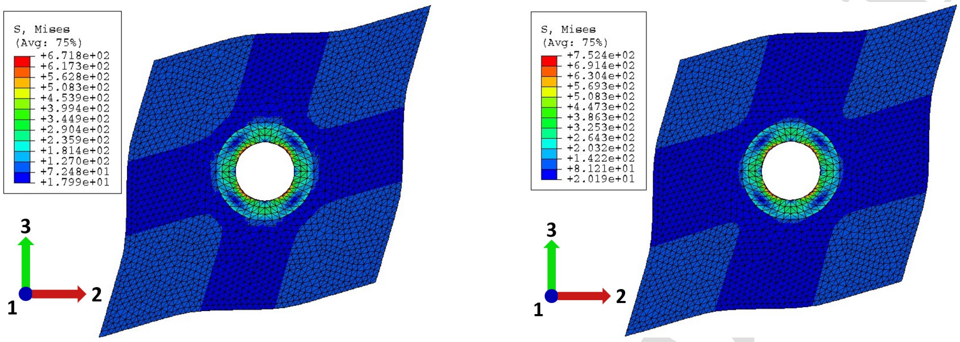

(a) Strain rate of 10^{-5} (1/s)

(b) Strain rate of 10^{-3} (1/s)

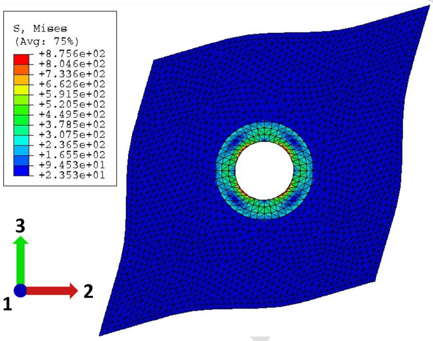

(c) Strain rate of 10^{-1} (1/s)

Figure 15: NCP: RVE response under shear loading at 23 plane at different strain rates: (a) 10^{-5} (1/s), (b) 10^{-3} (1/s), and (c) 10^{-1} (1/s).

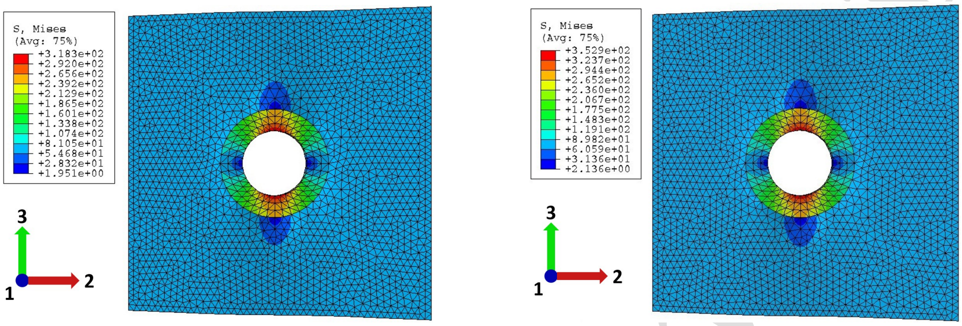

(a) Strain rate of 10^{-5} (1/s)

(b) Strain rate of 10^{-3} (1/s)

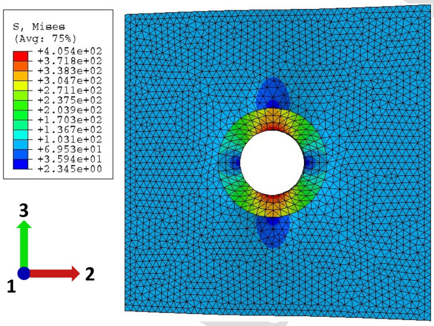

(c) Strain rate of 10^{-1} (1/s)

Figure 16: NCP: RVE response for shear loading at 13 plane at different strain rates: (a) 10^{-5} (1/s), (b) 10^{-3} (1/s), and (c) 10^{-1} (1/s).

Given the curves depicted in figures 12 and 13, the phenomenological behavior law of subsection 3.1, that considers 17 material parameters is employed. These include μ_{ax}, μ_{tr}, K, l, n, Y^t, Q_1^t, Q_2^t, K_a^t, N_a^t, b^t, Y^a, Q_1^a, Q_2^a, K_a^a, N_a^a, and b^a. For the identification of these material constants, two steps are considered. Since the hydrostatic response is purely elastic, an elastic homogenization using the Mori-Tanaka method [43] permits to identify the parameters K, l, and n. In the next step, the viscoplastic properties and the two shear moduli were determined from the curves presented in figures 12 and 13. Their estimation is achieved through reverse engineering approach analogous to the one used for the pure matrix material properties. The table 4 presents the equivalent properties of the nanocomposite interphase.

K (GPa)	l (GPa)	n (GPa)	μ^{tr} (MPa)	Y^t	Q_1^t	Q_2^t
3.8	2.32	74.53	1321.97	8.73	65.15	21.8
K_a^t (GPa)	N_a^t	b^t	μ^{ax} (MPa)	Y^a	Q_1^a	Q_2^a
22.7	10.7	116.3	1357.54	10.35	66.41	19.86
K_a^a (GPa)	N_a^a	b^a				
23.69	11.4	99.4				

Table 4: Effective properties of the nanocomposite (NCP) obtained via periodic homogenization at the scale of the NCP.

To accurately capture the mechanical behavior of the fuzzy fiber composites, two distinct homogenization strategies were adopted. The first approach considers all phases of the composite, including the main fiber, the CNT-reinforced interphase, the coating and the surrounding matrix, ensuring that each constituent's contribution to the overall mechanical response is explicitly accounted for. The second approach utilizes the equivalent fiber concept, where all phases except the matrix are replaced by a single homogenized equivalent fiber.

4.2. Mesoscale homogenization: Properties of the fuzzy fiber composite

After the equivalent properties of the nanocomposite interphase are determined, a damaged coating around the NCP needs to be defined prior to

---

the homogenization of the overall fuzzy fiber composite. This coating represents a region where damage manifests through the formation of spherical microvoids or microcracks. The coating is made of a material behaving as viscoplastic media (VPD), where the damage is considered discrete, as described in subsection 3.2. The properties of the coating, listed in the table 5, are taken from the work of Chen et al [44].

The overall fuzzy fiber composite's RVE can be described directly in the Cartesian coordinates as a four-phase medium, consisting of the main fiber, nanocomposite interphase layer, coating layer, and the surrounding matrix. In the same spirit as the microscale homogenization, the mesoscale periodic homogenization is performed on the tetragonal arrangement of the coated fiber, as shown in Figure 5. The unit cell has finite dimensions, and has been modeled as a rectangular prism with dimensions $14.56\,\mu\text{m} \times 14.56\,\mu\text{m} \times 0.1\,\mu\text{m}$. Important volume fractions for this analysis are provided in Appendix B.

Property of the coating	**Coating**
E (GPa)	2.99
ν	0.33
Y (MPa)	21.7
Q_1 (MPa)	0
Q_2 (MPa)	37.7
K_a (MPa.s$^{1/Na}$)	42.8
N_a	11.2
b	106.6
γ_{max}	0.99
σ_a	0
$\sigma_c(MPa)$	52.2
k	0.62
μ^{tr}	1125.4
μ^{ax}	1125.4
K^{tr}	3310.04
l	2184.62
n	4435.4
ϕ_1	0.39
ϕ_2	0.67

Table 5: Material properties of the coating identified using Levenberg-Marquardt (Chen et al [44]).

Figure 17 shows the shear deformation results of the fuzzy fiber composite at the 1-2 plane.

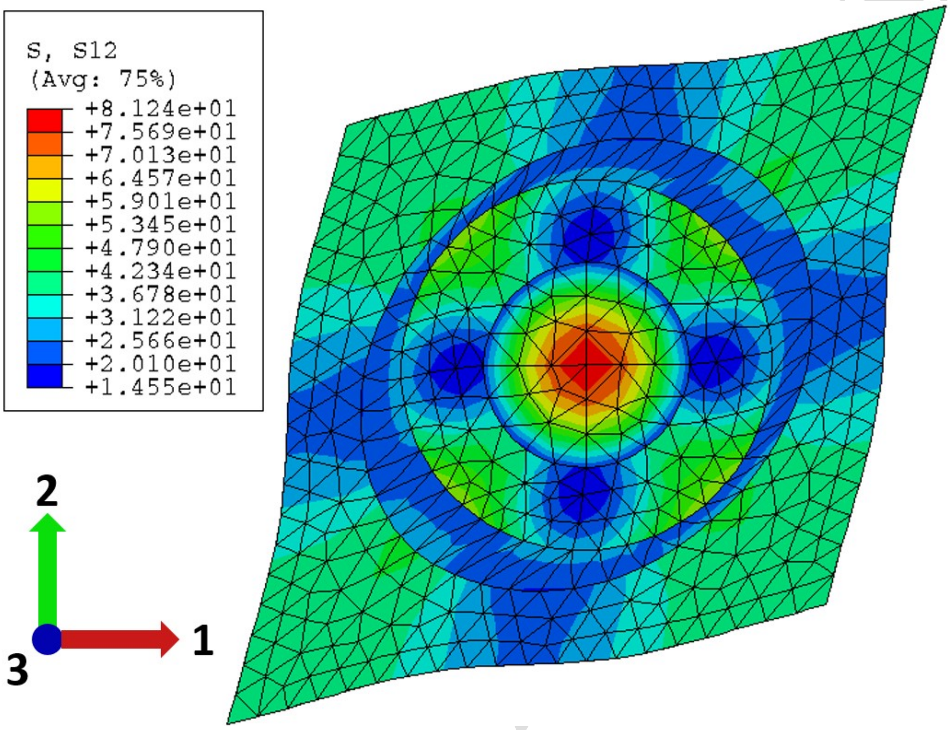

Figure 17: Shear deformation results of the fuzzy fiber composite on the 1-2 plane, showing stress distribution within the four-phase medium: the main fiber, nanocomposite interphase layer, damaged coating layer, and surrounding matrix under periodic boundary conditions.

Figure 18 presents the stress strain response of the fuzzy fiber composite RVE with the four phases.

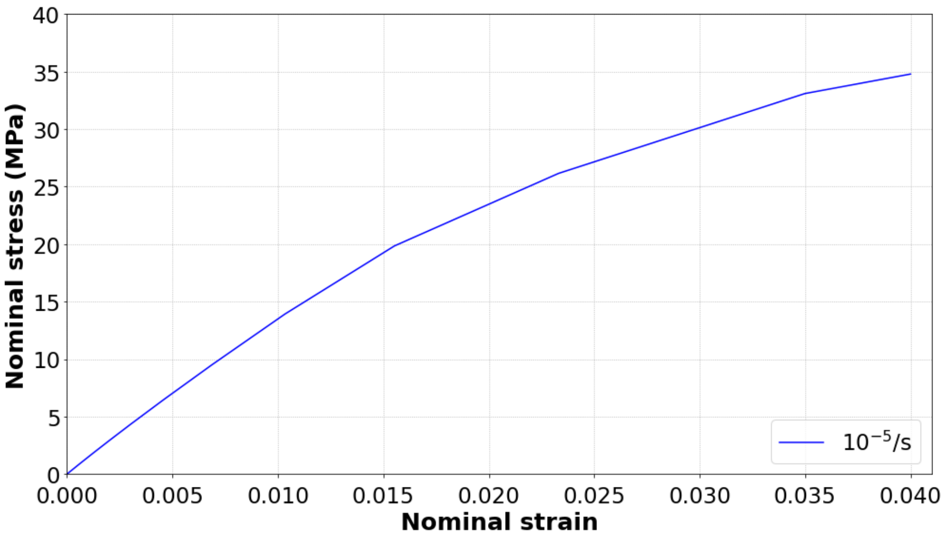

Figure 18: Shear stress-shear strain response of the fuzzy fiber composite with the four phases at a strain rate of $10^{-5}\,\mathrm{s}^{-1}$.

4.3. Mesoscale homogenization: Properties of the equivalent fiber

In this subsection, the complex system of inhomogeneities, consisting of the fiber, the nanocomposite interphase (NCP), and the coating, is replaced by a single equivalent inhomogeneity, referred to as the equivalent fiber (Figure 19). This substitution is achieved by employing the combined CCA/TFA approach discussed in subsections 3.3 and 3.4.

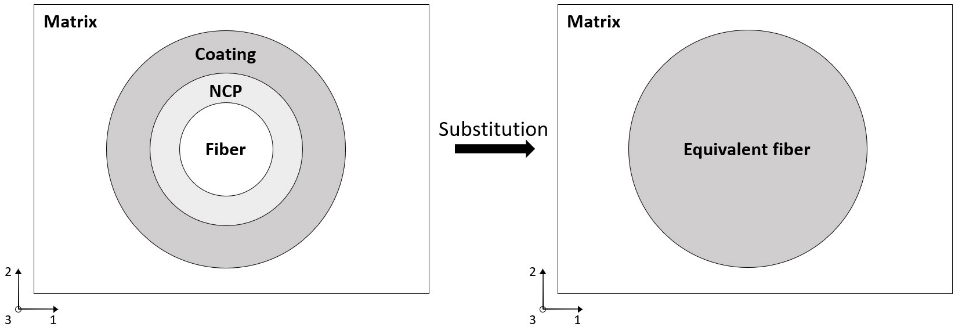

Figure 19: Schematic representation of the substitution process used to simplify the analysis of the composite system. The fiber, nanocomposite interphase (NCP), and coating are replaced by an equivalent inhomogeneity, referred to as the equivalent fiber.

For the numerical implementation, the material properties of each phase, necessary for accurately defining the overall response of the equivalent fiber, are listed in Tables 2, 3, 4 and 5. Important volume fractions for this analysis are provided in Appendix B.

For the equivalent fiber, a UMAT (User Material Subroutine) is employed with a clearly defined structure. This structure includes a separate return mapping algorithm, tangent modulus, and secant modulus to handle inelastic stress. This comprehensive UMAT approach ensures accurate simulation of the fiber's behavior under various loading conditions.

Figure 20 shows the result of shear test on the 1-2 plane of the equivalent fiber in the global reference of the composite.

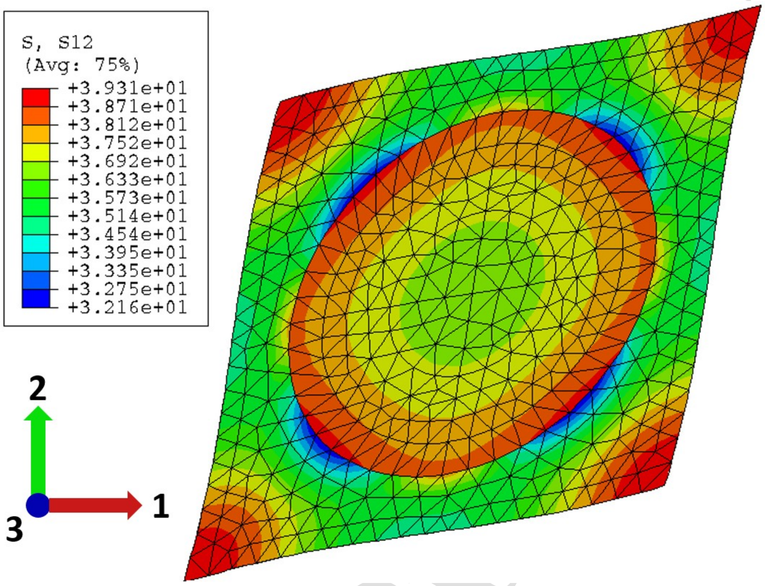

Figure 20: Shear test deformation on the 1-2 plane of the equivalent fiber, illustrating the distribution of von Mises stress.

Figure 21 compares the nominal stress-strain responses of the "Equivalent Fiber" and the "Fuzzy Fiber (consisting of all the four Phases)" under a nominal strain rate of $10^{-5}\,\mathrm{s}^{-1}$. The good agreement between the curves highlights the accuracy of the equivalent fiber modeling approach. However, a slight divergence is observed in the highly nonlinear region, which can be attributed to the adopted meshing strategy and the inherent approximations in the modeling method. It should be noted that the number of elements was obtained by a convergence analysis of the mesh.

For the sake of clarity and to improve the readability of all the previous modeling steps, Figure 22 provides the schematic workflow of the hierarchical modeling adopted for CNT-coated fuzzy fiber composites, accounting for viscoplasticity and discrete interfacial damage.

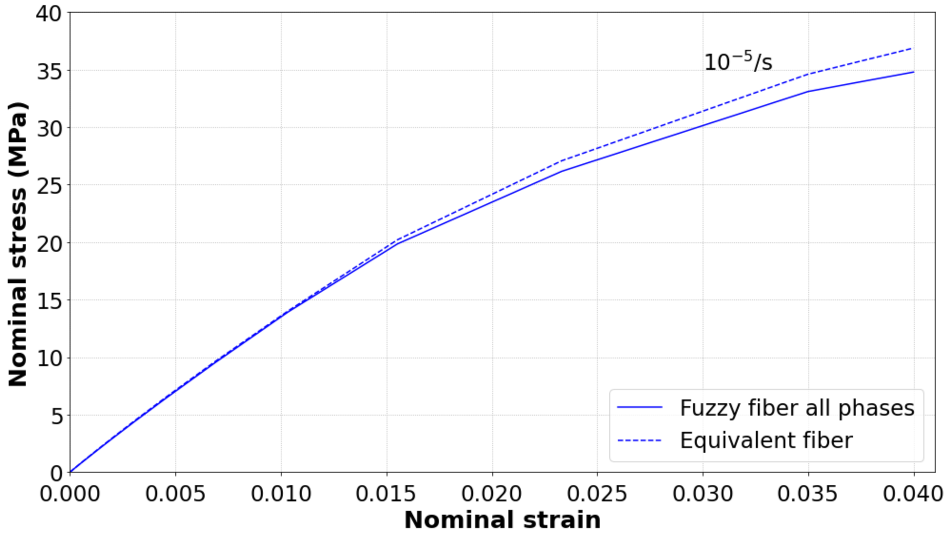

Figure 21: Comparison of the shear stressshear strain response between the equivalent fiber and the full fuzzy fiber composite, including all the four phases, at a strain rate of $10^{-5}\,\mathrm{s}^{-1}$.

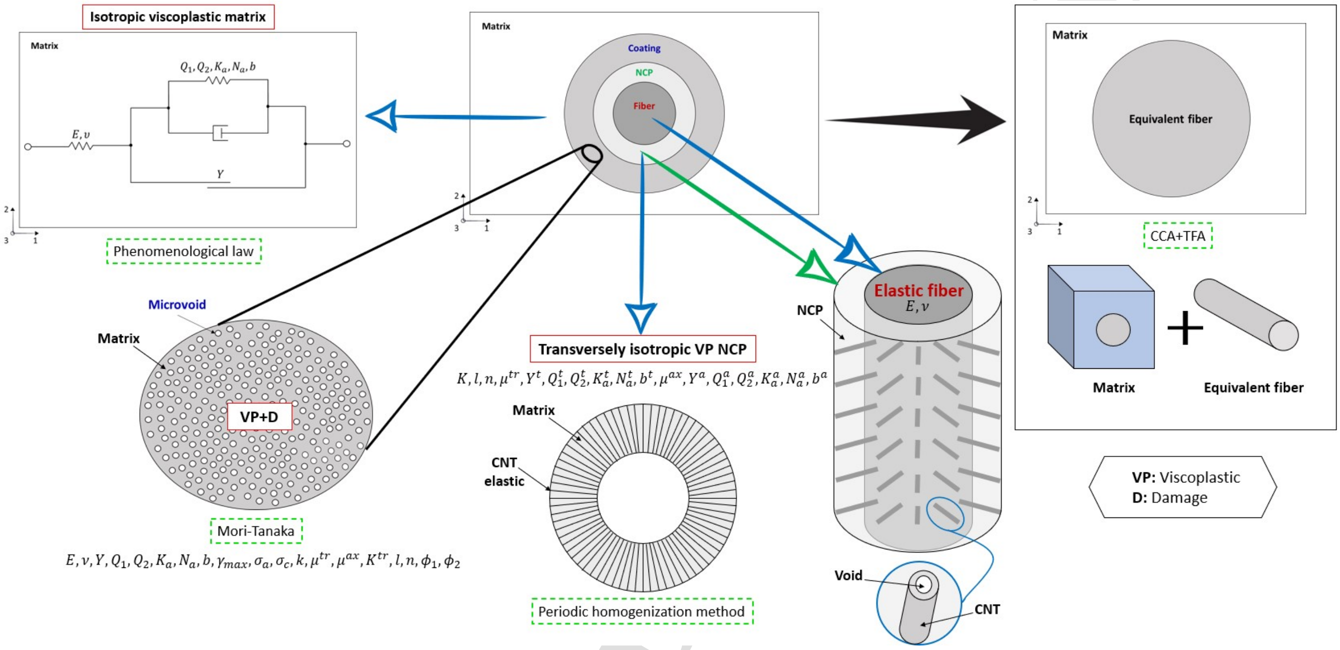

Figure 22: Graphical abstract of the multiscale model adopted for CNT-coated fuzzy fiber composites, accounting for viscoplasticity and discrete interfacial damage. The approach integrates a phenomenological law for the matrix, Mori-Tanaka and periodic homogenization methods for the coating and NCP, respectively, along with CCA and TFA techniques to determine the overall material behavior.

5. Parametric study

Since the numerical results demonstrate that the equivalent fiber approach provides good accuracy, the subsequent parametric analyses will be performed using the equivalent fiber concept. The scope of this section is to investigate the impact of varying key parameters on the equivalent fiber and, consequently, on the overall properties of the composite material. Material properties identified in the previous section are used for the analyses.

It should be noted that in all loading conditions, the strain rate is set to $10^{-5}/s$. The dimensions of the RVE adopted for the parametric analysis of the parameters ϕ_1 and ϕ_2 are $14.56 \times 14.56 \times 0.1$. The equivalent fiber model is subjected to nonlinear deformation at different values of the parameters ϕ_1, ϕ_2 and the volume fraction of the matrix c_m. The results are plotted as nominal stress-strain curves and depicted in figures 23 and 25. The objective is to determine if these parameters influence the distribution of various properties under loading conditions. The calculations will be divided into three distinct cases, as described below.

5.1. Case 1: Variation of ϕ_2 with ϕ_1 constant

In the first case, the value of ϕ_1 is kept constant while ϕ_2 obtains four different values: 0.3, 0.4, 0.5 and 0.67. The results are summarized in figures 23 and 24.

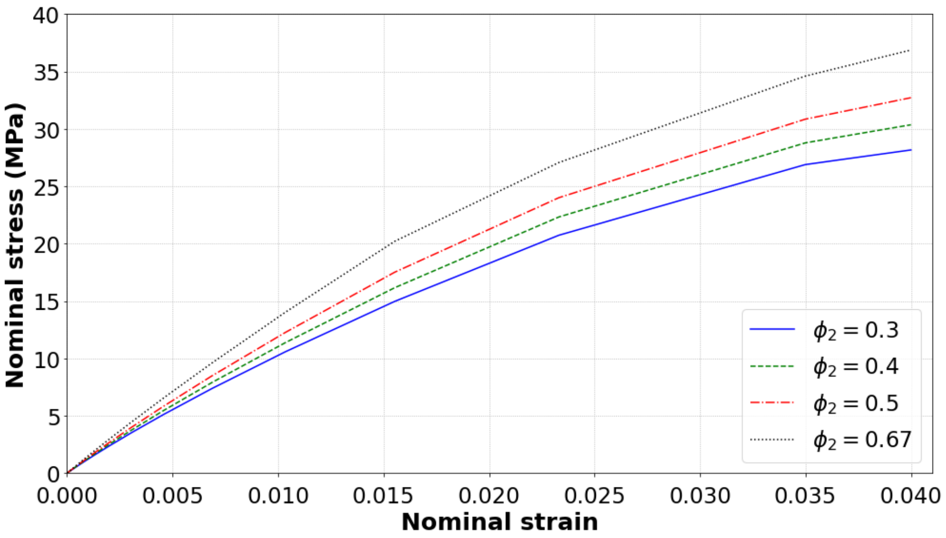

Figure 23: Nominal stress-strain curves of in-plane shear loading (1-2) for the equivalent fiber model under varying values of ϕ_2, while ϕ_1 is held constant. The curves correspond to different ϕ_2 values: 0.3, 0.4, 0.5, and 0.67. All simulations are performed at a strain rate of $10^{-5}\,\mathrm{s}^{-1}$.

The results show a significant influence of ϕ_2 on the mechanical response of the equivalent fiber. Higher values of ϕ_2 correspond to increased nominal stress levels at the same strain, indicating greater stiffness in the equivalent fiber.

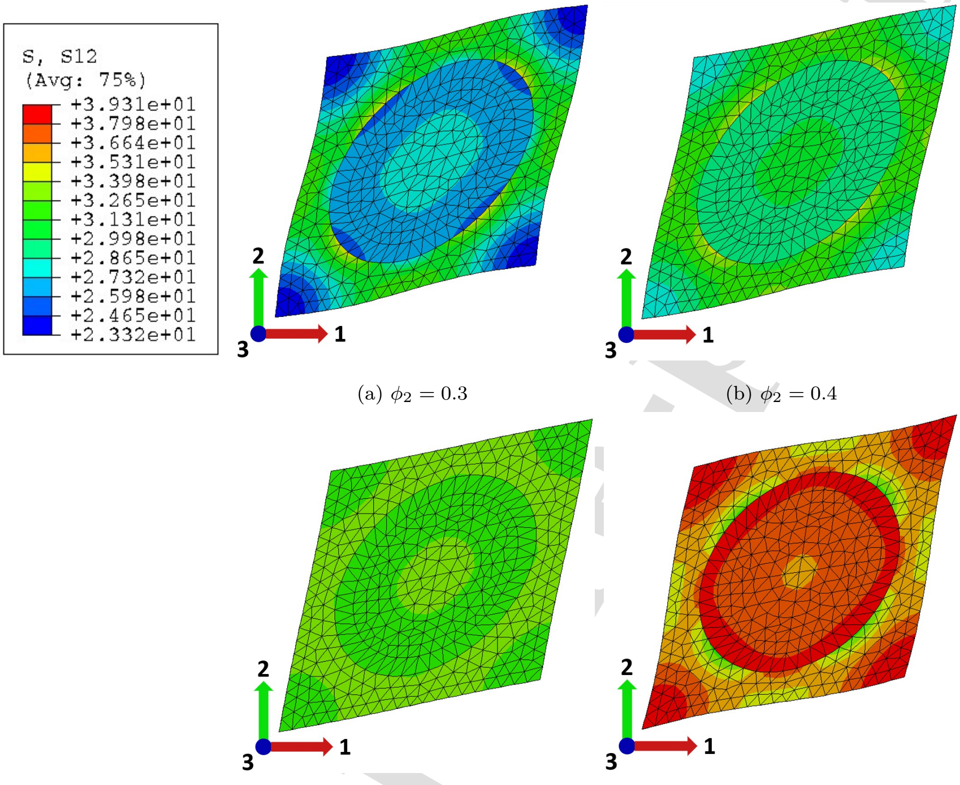

(a) $\phi_2 = 0.3$

(b) $\phi_2 = 0.4$

(c) $\phi_2 = 0.5$

(d) $\phi_2 = 0.67$

Figure 24: Shear stress-shear strain distribution on the equivalent fiber model under varying parameter ϕ_2, showcasing the evolution of shear stress for (a) $\phi_2 = 0.3$, (b) $\phi_2 = 0.4$, (c) $\phi_2 = 0.5$, and (d) $\phi_2 = 0.67$. All simulations are performed at a strain rate of $10^{-5}\,\mathrm{s}^{-1}$.

5.2. Case 2: Variation of ϕ_1 with ϕ_2 constant

In the second case, ϕ_2 is held constant, and ϕ_1 obtains four different values: 0.3, 0.39, 0.5 and 0.6. The results are summarized in figures 25 and 26.

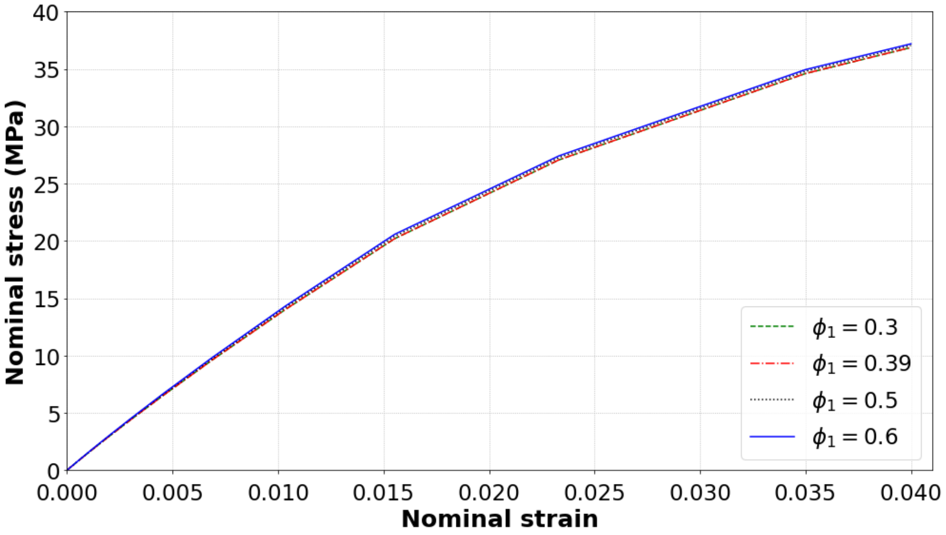

Figure 25: Nominal stress-strain curves of in-plane shear loading (1-2) for the equivalent fiber model under varying values of ϕ_1, while ϕ_2 is held constant. The curves correspond to different ϕ_1 values: 0.3, 0.39, 0.5, and 0.6. All simulations are conducted at a strain rate of $10^{-5}\,\mathrm{s}^{-1}$.

The results show that variations in ϕ_1 have a negligible effect on the nominal stress-strain response. All the curves are closely aligned across all ϕ_1 values, indicating that the equivalent fiber's mechanical response is not significantly influenced by changes in ϕ_1 under these loading conditions.

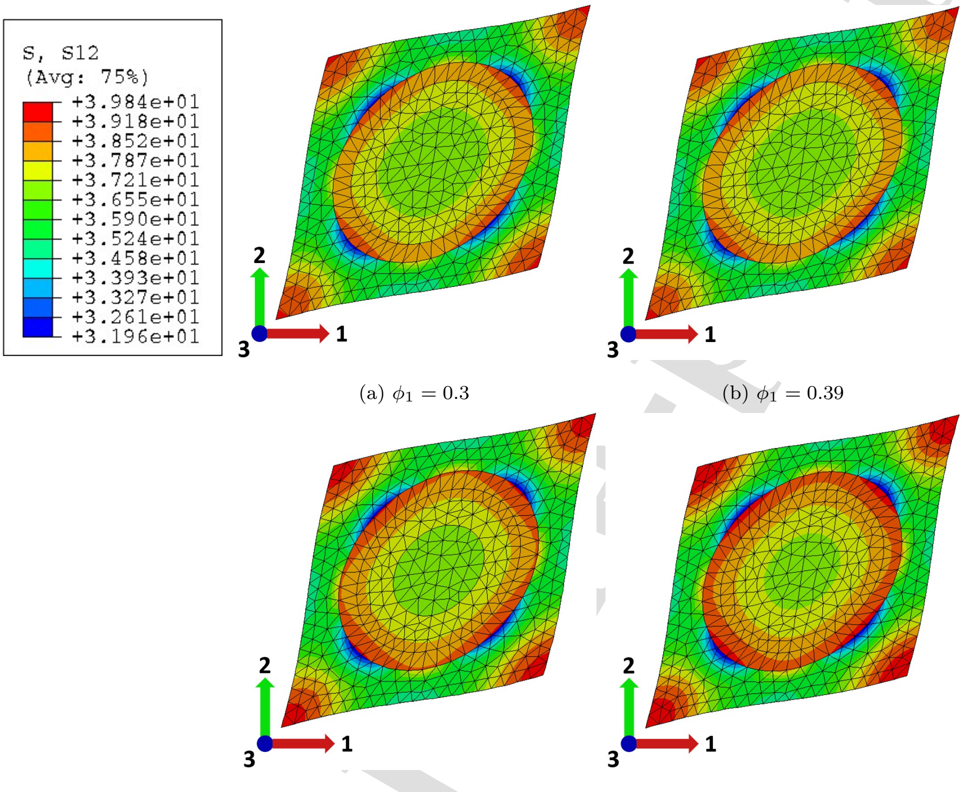

(a) $\phi_1 = 0.3$ (b) $\phi_1 = 0.39$

(c) $\phi_1 = 0.5$ (d) $\phi_1 = 0.6$

Figure 26: Shear stress-shear strain distribution on the equivalent fiber model under varying parameter ϕ_1, showcasing the evolution of shear stress for (a) $\phi_1 = 0.3$, (b) $\phi_1 = 0.39$, (c) $\phi_1 = 0.5$, and (d) $\phi_1 = 0.6$. All simulations are performed at a strain rate of $10^{-5}\,\mathrm{s}^{-1}$.

5.3. *Case 3: Variation of the Matrix Volume Fraction*

For the third case, the values of ϕ_1 and ϕ_2 are held constant at values 0.39 and 0.67, respectively, while the size of the equivalent fiber is altered by varying the matrix volume fraction. This leads to an analysis on how the matrix's volume fraction affects the overall properties of the composite material. The dimensions of the Representative Volume Element (RVE) adopted for this parametric study are $1 \times 1 \times 0.1$. The analysis is carried out for five distinct values of the parameter c_m: $c_m = 0.3$, $c_m = 0.4$, $c_m = 0.55$, $c_m = 0.6$, and $c_m = 0.8$ (figures 27 and 28).

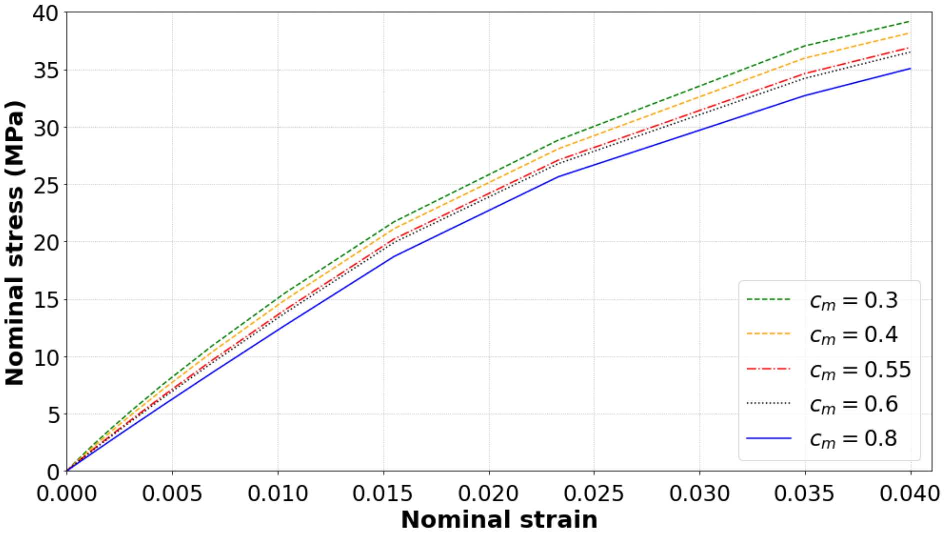

Figure 27: Nominal stress-strain curves of in-plane shear loading (1-2) for the equivalent fiber model under varying values of c_m. The curves correspond to different c_m values: 0.3, 0.4, 0.55, 0.6, and 0.8. All simulations are conducted at a strain rate of $10^{-5}\,\mathrm{s}^{-1}$.

It is observed that, the nominal stress-strain behavior of the equivalent fiber model varies significantly with changes in the matrix volume fraction c_m. As c_m decreases, the nominal stress for a given strain increases, reflecting an enhancement in the stiffness of the composite material. This response can be attributed to the reduced proportion of the matrix, which typically exhibits lower mechanical properties compared to the equivalent fiber. Consequently, the overall load-bearing capacity and rigidity of the composite are improved as the matrix volume fraction decreases.

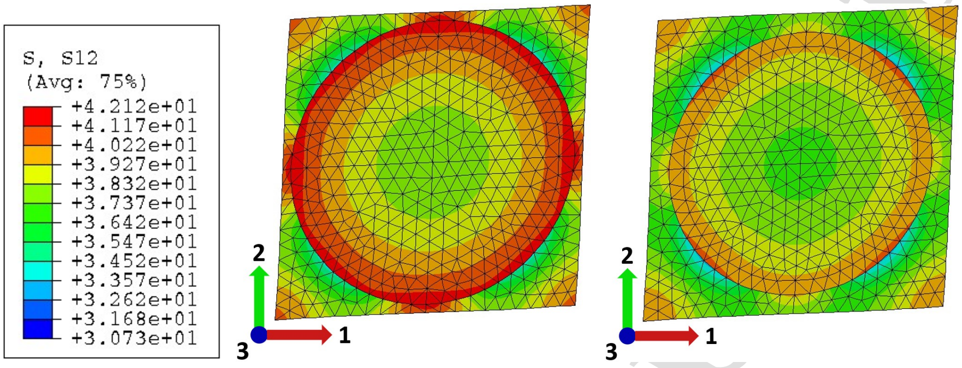

(a) $c_m = 0.3$ (b) $c_m = 0.4$

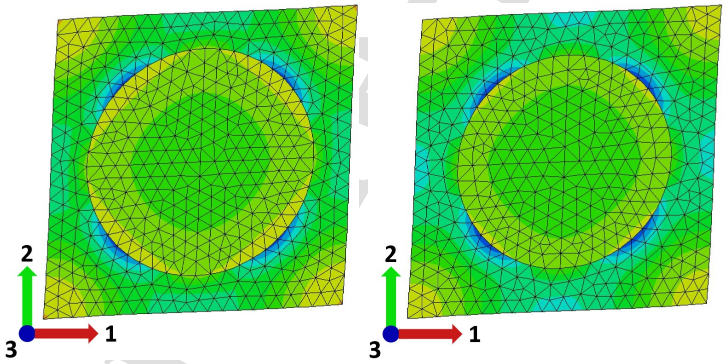

(c) $c_m = 0.55$ (d) $c_m = 0.6$

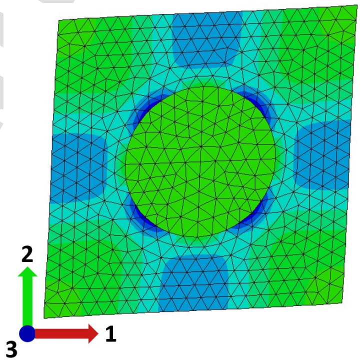

(e) $c_m = 0.8$

Figure 28: Shear stress-shear strain distribution on the equivalent fiber model under varying parameter c_m, showcasing the evolution of shear stress for (a) $c_m = 0.3$, (b) $c_m = 0.4$, (c) $c_m = 0.55$, (d) $c_m = 0.6$, and (e) $c_m = 0.8$. All simulations are performed at a strain rate of $10^{-5}\,\mathrm{s}^{-1}$.

6. Summary and conclusions

Fuzzy fiber composites, which consist of radially aligned CNTs coating the main fibers, represent a promising class of hierarchically reinforced heterogeneous materials. This study presents a novel and comprehensive micromechanical framework for modeling and optimizing these composites. A key contribution of this work lies in the incorporation of a viscoplastic isotropic matrix model, alongside a damage mechanism introduced via microvoids in the coating. This damage model is crucial for accurately predicting the materials performance under stress as well as the damage accumulation in such a composite.

To ensure a rigorous analysis, multiple homogenization techniques such as the Composite Cylinder Assemblage (CCA), Transformation Field Analysis (TFA), and periodic homogenization were employed at various scales. A comparative analysis between the shear stress-strain response of the equivalent fiber and the full fuzzy fiber composite reveals a high degree of correlation. Minor deviations observed in the nonlinear regime are likely attributable to meshing choices and the inherent approximations of the model itself.

A significant advancement in this research is the development of an equivalent fiber model that effectively reduces the complexity of the multi-phase composite structure, allowing for more efficient parametric analyses. By substituting the original multiple material phases with a single equivalent fiber, we streamline the investigation of key factors that influence the composites behavior. This simplification not only enhances the efficiency of the modeling process but also opens the door for integrating machine learning algorithms to further refine and optimize the material properties.

The results presented in this work provide new insights into the behavior of unidirectional fuzzy fiber composites, particularly in the context of a viscoplastic matrix. The numerical examples validate the approach and emphasize its potential for broader application. Future work will focus on conducting an extensive parametric investigation across a range of fuzzy fiber configurations. Additionally, the method will be applied to more complex nonlinear composite systems, further demonstrating its capabilities and potential real-world applications.

Declaration of competing interest

The authors declare that they have no known competing financial interests or personal relationships that could have appeared to influence the work reported in this paper.

Acknowledgments

The authors gratefully acknowledge the use of the Cassiopee Arts et Métiers Institute of Technology HPC Center made available for conducting the research reported in this paper.

References

[1] S. Iijima, Helical microtubules of graphitic carbon, Nature 354 (1991) 56–58. doi:`10.1038/354056a0`.

[2] G. Chatzigeorgiou, G. D. Seidel, D. C. Lagoudas, Effective mechanical properties of fuzzy fiber composites, Composites Part B: Engineering

---

43 (2012) 2577–2593. doi:`https://doi.org/10.1016/j.compositesb.2012.03.001`, homogenization and Micromechanics of Smart and Multifunctional Materials.

[3] S. Kundalwal, M. Ray, Effective properties of a novel composite reinforced with short carbon fibers and radially aligned carbon nanotubes, Mechanics of Materials 53 (2012) 47–60. doi:`https://doi.org/10.1016/j.mechmat.2012.05.008`.

[4] J. Hone, M. Whitney, A. Zettl, Thermal conductivity of single-walled carbon nanotubes, Synthetic Metals 103 (1999) 2498–2499. doi:`https://doi.org/10.1016/S0379-6779(98)01070-4`, international Conference on Science and Technology of Synthetic Metals.

[5] L. Tian, G. Wang, H. Zhao, M. Yuan, Y. Peng, J. Chen, A novel multiscale semi-analytical approach for thermal properties of fuzzy fiber reinforced composites, Composite Structures 275 (2021) 114424. doi:`https://doi.org/10.1016/j.compstruct.2021.114424`.

[6] H. Qian, E. S. Greenhalgh, M. S. P. Shaffer, A. Bismarck, Carbon nanotube-based hierarchical composites: a review, J. Mater. Chem. 20 (2010) 4751–4762. doi:`10.1039/C000041H`.

[7] Q. Song, K.-z. Li, H.-l. Li, H.-j. Li, C. Ren, Grafting straight carbon nanotubes radially onto carbon fibers and their effect on the mechanical properties of carbon/carbon composites, Carbon 50 (2012) 39493952. doi:`10.1016/j.carbon.2012.03.023`.

---

[8] J. Sebastian, N. Schehl, M. Bouchard, M. Boehle, L. Li, A. Lagounov, K. Lafdi, Health monitoring of structural composites with embedded carbon nanotube coated glass fiber sensors, Carbon 66 (2014) 191–200. doi:`https://doi.org/10.1016/j.carbon.2013.08.058`.

[9] D. B. Anthony, H. Qian, A. J. Clancy, E. S. Greenhalgh, A. Bismarck, M. S. P. Shaffer, Applying a potential difference to minimise damage to carbon fibres during carbon nanotube grafting by chemical vapour deposition, Nanotechnology 28 (2017) 305602. doi:`10.1088/1361-6528/aa783f`.

[10] Q. Li, J. S. Church, M. Naebe, B. L. Fox, A systematic investigation into a novel method for preparing carbon fibrecarbon nanotube hybrid structures, Composites Part A: Applied Science and Manufacturing 90 (2016) 174–185. doi:`https://doi.org/10.1016/j.compositesa.2016.05.004`.

[11] Y. Rao, J. Ban, S. Yao, K. Wang, N. Wei, Y. Lu, S. Ahzi, A hierarchical prediction scheme for effective properties of fuzzy fiber reinforced composites with two-scale interphases: Based on three-phase bridging model, Mechanics of Materials 152 (2021) 103653. doi:`https://doi.org/10.1016/j.mechmat.2020.103653`.

[12] G. Chatzigeorgiou, Y. Efendiev, D. C. Lagoudas, Homogenization of aligned fuzzy fiber composites, International Journal of Solids and Structures 48 (2011) 2668–2680. doi:`https://doi.org/10.1016/j.ijsolstr.2011.05.011`.

[13] G. Chatzigeorgiou, F. Meraghni, N. Charalambakis, A. Benaarbia, Multiscale modeling accounting for inelastic mechanisms of fuzzy fiber composites with straight or wavy carbon nanotubes, International Journal of Solids and Structures 202 (2020) 39–57. doi:`https://doi.org/10.1016/j.ijsolstr.2020.05.015`.

[14] Q. Chen, G. Chatzigeorgiou, F. Meraghni, Hybrid hierarchical homogenization theory for unidirectional cnts-coated fuzzy fiber composites undergoing inelastic deformations, Composites Science and Technology 215 (2021) 109012. doi:`https://doi.org/10.1016/j.compscitech.2021.109012`.

[15] S. Kundalwal, M. Ray, Effect of carbon nanotube waviness on the effective thermoelastic properties of a novel continuous fuzzy fiber reinforced composite, Composites Part B: Engineering 57 (2014) 199–209. doi:`https://doi.org/10.1016/j.compositesb.2013.10.003`.

[16] S. Kundalwal, S. Meguid, Micromechanics modelling of the effective thermoelastic response of nano-tailored composites, European Journal of Mechanics - A/Solids 53 (2015) 241–253. doi:`https://doi.org/10.1016/j.euromechsol.2015.05.008`.

[17] G. D. Seidel, G. Chatzigeorgiou, X. Ren, D. C. Lagoudas, Multiscale Modeling of Multifunctional Fuzzy Fibers based on Multi-Walled Carbon Nanotubes, in: K. I. Tserpes, N. P. Silvestre (Eds.), Modeling of Carbon Nanotubes, Graphene and their Composites, volume 188 of *Springer Series in Materials Science*, Springer International Publishing, Cham, 2014, pp. 135–176. doi:`10.1007/978-3-319-01201-8_5`.

[18] S. Dhala, M. Ray, Micromechanics of piezoelectric fuzzy fiber-reinforced composite, Mechanics of Materials 81 (2015) 1–17. doi:`https://doi.org/10.1016/j.mechmat.2014.10.004`.

[19] R. Li, N. Lachman, P. Florin, H. D. Wagner, B. L. Wardle, Hierarchical carbon nanotube carbon fiber unidirectional composites with preserved tensile and interfacial properties, Composites Science and Technology 117 (2015) 139–145. doi:`https://doi.org/10.1016/j.compscitech.2015.04.014`.

[20] M. Barral, G. Chatzigeorgiou, F. Meraghni, R. Léon, Homogenization using modified mori-tanaka and tfa framework for elastoplastic-viscoelastic-viscoplastic composites: Theory and numerical validation, International Journal of Plasticity 127 (2020) 102632. doi:`https://doi.org/10.1016/j.ijplas.2019.11.011`.

[21] Q. Chen, G. Chatzigeorgiou, F. Meraghni, Extended mean-field homogenization of viscoelastic-viscoplastic polymer composites undergoing hybrid progressive degradation induced by interface debonding and matrix ductile damage, International Journal of Solids and Structures 210-211 (2021) 1–17. doi:`https://doi.org/10.1016/j.ijsolstr.2020.11.017`.

[22] Z. Hashin, B. W. Rosen, The Elastic Moduli of Fiber-Reinforced Materials, Journal of Applied Mechanics 31 (1964) 223–232. doi:`10.1115/1.3629590`.

[23] R. Malekimoghadam, U. Icardi, Prediction of mechanical properties of

---

carbon nanotubecarbon fiber reinforced hybrid composites using multi-scale finite element modelling, Composites Part B: Engineering 177 (2019) 107405. doi:`https://doi.org/10.1016/j.compositesb.2019.107405`.

[24] X. Ren, J. Burton, G. D. Seidel, K. Lafdi, Computational multiscale modeling and characterization of piezoresistivity in fuzzy fiber reinforced polymer composites, International Journal of Solids and Structures 54 (2015) 121–134. doi:`https://doi.org/10.1016/j.ijsolstr.2014.10.034`.

[25] Q. Chen, J. Zhu, W. Tu, G. Wang, A tangent finite-volume direct averaging micromechanics framework for elastoplastic porous materials: Theory and validation, International Journal of Plasticity 139 (2021) 102968. doi:`https://doi.org/10.1016/j.ijplas.2021.102968`.

[26] Z. He, M.-J. Pindera, Finite volume based asymptotic homogenization theory for periodic materials under anti-plane shear, European Journal of Mechanics - A/Solids 85 (2021) 104122. doi:`https://doi.org/10.1016/j.euromechsol.2020.104122`.

[27] M. Schneider, A review of nonlinear fft-based computational homogenization methods, Acta Mechanica 232 (2021) 1–50. doi:`10.1007/s00707-021-02962-1`.

[28] G. Chatzigeorgiou, N. Charalambakis, Y. Chemisky, F. Meraghni, Periodic homogenization for fully coupled thermomechanical modeling of dissipative generalized standard materials, International Journal of

---

Plasticity 81 (2016) 18–39. doi:https://doi.org/10.1016/j.ijplas.2016.01.013.

[29] Q. Chen, G. Wang, X. Chen, J. Geng, Finite-volume homogenization of elastic/viscoelastic periodic materials, Composite Structures 182 (2017) 457–470. doi:https://doi.org/10.1016/j.compstruct.2017.09.044.

[30] S. Kundalwal, M. Ray, Effective properties of a novel continuous fuzzy-fiber reinforced composite using the method of cells and the finite element method, European Journal of Mechanics - A/Solids 36 (2012) 191–203. doi:https://doi.org/10.1016/j.euromechsol.2012.03.006.

[31] S. Gajek, M. Schneider, T. Böhlke, On the micromechanics of deep material networks, Journal of the Mechanics and Physics of Solids 142 (2020) 103984. doi:https://doi.org/10.1016/j.jmps.2020.103984.

[32] J. Wang, K. Liew, On the study of elastic properties of cnt-reinforced composites based on element-free mls method with nanoscale cylindrical representative volume element, Composite Structures 124 (2015) 1–9. doi:https://doi.org/10.1016/j.compstruct.2015.01.006.

[33] A. Hernández-Pérez, F. Aviles, Modeling the influence of interphase on the elastic properties of carbon nanotube composites, Computational Materials Science - COMPUT MATER SCI 47 (2010) 926–933. doi:10.1016/j.commatsci.2009.11.025.

[34] G. Seidel, D. Lagoudas, Micromechanical analysis of the effective elastic properties of carbon nanotube reinforced composites, Mechanics of Materials 38 (2006) 884–907. doi:10.1016/j.mechmat.2005.06.029.

[35] M. Hassanzadeh-Aghdam, M. Mahmoodi, R. Ansari, Micromechanics-based characterization of mechanical properties of fuzzy fiber-reinforced composites containing carbon nanotubes, Mechanics of Materials 118 (2018) 31–43. doi:`https://doi.org/10.1016/j.mechmat.2017.12.003`.

[36] P. Li, Y. Guo, V. Shim, A constitutive model for transversely isotropic material with anisotropic hardening, International Journal of Solids and Structures 138 (2018) 40–49. doi:`https://doi.org/10.1016/j.ijsolstr.2017.12.026`.

[37] N. Nik Long, A. Khaldjigitov, U. Adambaev, On the constitutive relations for isotropic and transversely isotropic materials, Applied Mathematical Modelling 37 (2013) 7726–7740. doi:`https://doi.org/10.1016/j.apm.2013.03.012`.

[38] S. Kundalwal, M. Ray, Micromechanical analysis of fuzzy fiber reinforced composites, International Journal of Mechanics and Materials in Design 7 (2011) 149–166. doi:`10.1007/s10999-011-9156-4`.

[39] J. Lemaitre, J. L. Chaboche, Mechanics of solid materials, Cambridge University Press, Cambridge, 2002.

[40] X. Poulain, A. Benzerga, R. Goldberg, Finite-strain elasto-viscoplastic behavior of an epoxy resin: Experiments and modeling in the glassy regime, International Journal of Plasticity 62 (2014) 138–161. doi:`https://doi.org/10.1016/j.ijplas.2014.07.002`.

---

[41] S. Community, Least squares optimization, 2025. URL: https://docs.scipy.org/doc/scipy/reference/generated/scipy.optimize.least_squares.html.

[42] H. Khatam, L. Chen, M.-J. Pindera, Elastic and plastic response of perforated metal sheets with different porosity architectures, Journal of Engineering Materials and Technology 131 (2009) 031015. doi:10.1115/1.3086405.

[43] G. Chatzigeorgiou, F. Meraghni, N. Charalambakis, Multiscale Modeling Approaches for Composites, Elsevier, 2021. doi:10.1016/c2019-0-05214-4.

[44] Q. Chen, G. Chatzigeorgiou, G. Robert, F. Meraghni, Viscoelastic-viscoplastic homogenization of short glass-fiber reinforced polyamide composites (PA66/GF) with progressive interphase and matrix damage: New developments and experimental validation, Mechanics of Materials 164 (2022) 104081. doi:https://doi.org/10.1016/j.mechmat.2021.104081.

[45] G. Chatzigeorgiou, N. Charalambakis, Y. Chemisky, F. Meraghni, Thermomechanical Behavior of Dissipative Composite Materials, ISTE-Elsevier, 2018. doi:10.1016/C2017-0-01481-7.

Appendix A

The stress rotation matrix $\boldsymbol{Q}_\sigma$ and the strain rotation matrix $\boldsymbol{Q}_\epsilon$, introduced in Equations 26 and 27, are defined as follows [43] [45]:

$$\boldsymbol{Q}_\epsilon = \begin{bmatrix} \cos^2\theta & \sin^2\theta & 0 & \cos\theta\sin\theta & 0 & 0 \\ \sin^2\theta & \cos^2\theta & 0 & -\cos\theta\sin\theta & 0 & 0 \\ 0 & 0 & 1 & 0 & 0 & 0 \\ -2\cos\theta\sin\theta & 2\cos\theta\sin\theta & 0 & -\sin^2\theta+\cos^2\theta & 0 & 0 \\ 0 & 0 & 0 & 0 & \cos\theta & \sin\theta \\ 0 & 0 & 0 & 0 & -\sin\theta & \cos\theta \end{bmatrix},$$

$$\boldsymbol{Q}_\sigma = \begin{bmatrix} \cos^2\theta & \sin^2\theta & 0 & 2\cos\theta\sin\theta & 0 & 0 \\ \sin^2\theta & \cos^2\theta & 0 & -2\cos\theta\sin\theta & 0 & 0 \\ 0 & 0 & 1 & 0 & 0 & 0 \\ -\cos\theta\sin\theta & \cos\theta\sin\theta & 0 & -\sin^2\theta+\cos^2\theta & 0 & 0 \\ 0 & 0 & 0 & 0 & \cos\theta & \sin\theta \\ 0 & 0 & 0 & 0 & -\sin\theta & \cos\theta \end{bmatrix}.$$

Appendix B

In Table 5, ϕ_1 and ϕ_2 represent the ratio of the fiber's area to the combined area of the fiber and NCP, and the ratio of the area of the fiber + NCP to the total area including the coating, respectively. They are defined as follows:

$$\phi_1 = \frac{(r_{fiber})^2}{(r_{NCP+fiber})^2}, \qquad \phi_2 = \frac{(r_{NCP+fiber})^2}{(r_{NCP+fiber+coating})^2}.$$

Equivalent fiber:

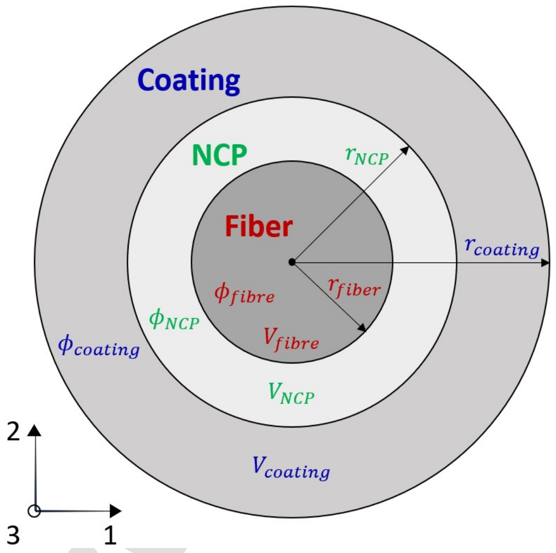

Figure 29: Schematic representation of the equivalent fiber model for the fuzzy fiber composite, showing the fiber core, the nanocomposite phase (NCP), and the coating layers with their respective radii ($r_{\text{fiber}}, r_{\text{NCP}}, r_{\text{coating}}$), volume fractions ($\phi_{\text{fiber}}, \phi_{\text{NCP}}, \phi_{\text{coating}}$), and volumes ($V_{\text{fiber}}, V_{\text{NCP}}, V_{\text{coating}}$).

The volume fraction of each phase in the equivalent fiber is

$$\phi_{fiber} = \phi_1\phi_2 = \frac{V_{fiber}}{V_{fiber} + V_{NCP} + V_{coating}},$$
$$\phi_{NCP} = \phi_2 - \phi_1\phi_2 = \frac{V_{NCP}}{V_{fiber} + V_{NCP} + V_{coating}},$$
$$\phi_{coating} = 1 - \phi_2 = \frac{V_{coating}}{V_{fiber} + V_{NCP} + V_{coating}}.$$

797 *Fuzzy fiber composite:*

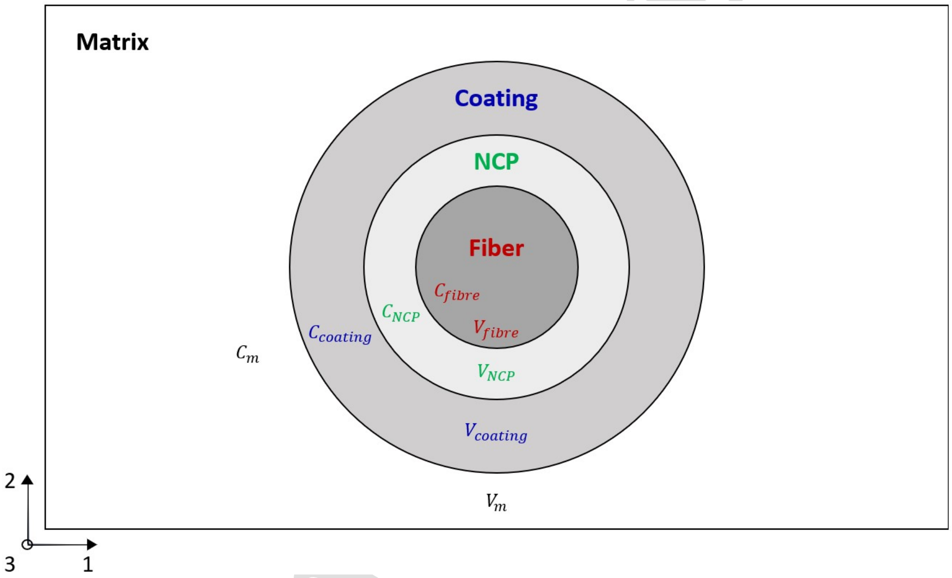

Figure 30: Schematic representation of the representative volume element (RVE) of the fuzzy fiber composite structure, illustrating its hierarchical organization into four main components: the fiber core, the nanocomposite phase (NCP), the coating layer, and the surrounding matrix. The respective volume fractions ($c_{\text{fiber}}, c_{\text{NCP}}, c_{\text{coating}}, c_m$) and volumes ($V_{\text{fiber}}, V_{\text{NCP}}, V_{\text{coating}}, V_m$) are indicated for each region.

798 The volume fractions of each component in the fuzzy fiber composite are
799 defined as follows

$$
\begin{aligned}
c_{fiber} &= \frac{V_{fiber}}{V_{fiber} + V_{NCP} + V_{coating} + V_m},\\
c_{NCP} &= \frac{V_{NCP}}{V_{fiber} + V_{NCP} + V_{coating} + V_m},\\
c_{coating} &= \frac{V_{coating}}{V_{fiber} + V_{NCP} + V_{coating} + V_m},\\
c_m &= \frac{V_m}{V_{fiber} + V_{NCP} + V_{coating} + V_m}.
\end{aligned}
$$

From these relations, it can be shown that

$$\phi_{fiber}(1 - c_m) = c_{fiber}.$$

and that

$$\frac{c_{fiber}}{\phi_{fiber}} = \frac{c_{NCP}}{\phi_{NCP}} = \frac{c_{coating}}{\phi_{coating}} = 1 - c_m.$$

Consequently, the individual volume fractions for each component can be expressed as

$$
\begin{aligned}
c_{fiber} &= (1 - c_m)\phi_1\phi_2,\\
c_{NCP} &= (1 - c_m)(\phi_2 - \phi_1\phi_2),\\
c_{coating} &= (1 - c_m)(1 - \phi_2).
\end{aligned}
$$

Highlights

- Multiscale framework for nonlinear fuzzy fiber composites.
- Hybrid technique combining full-field and mean-field homogenization strategies.
- Accounting for matrix viscoplasticity and interfacial damage.
- At microscale the matrix-CNTs medium has transversely isotropic viscoplastic behavior.
- Equivalent fiber approach using micromechanics and Transformation Field Analysis.

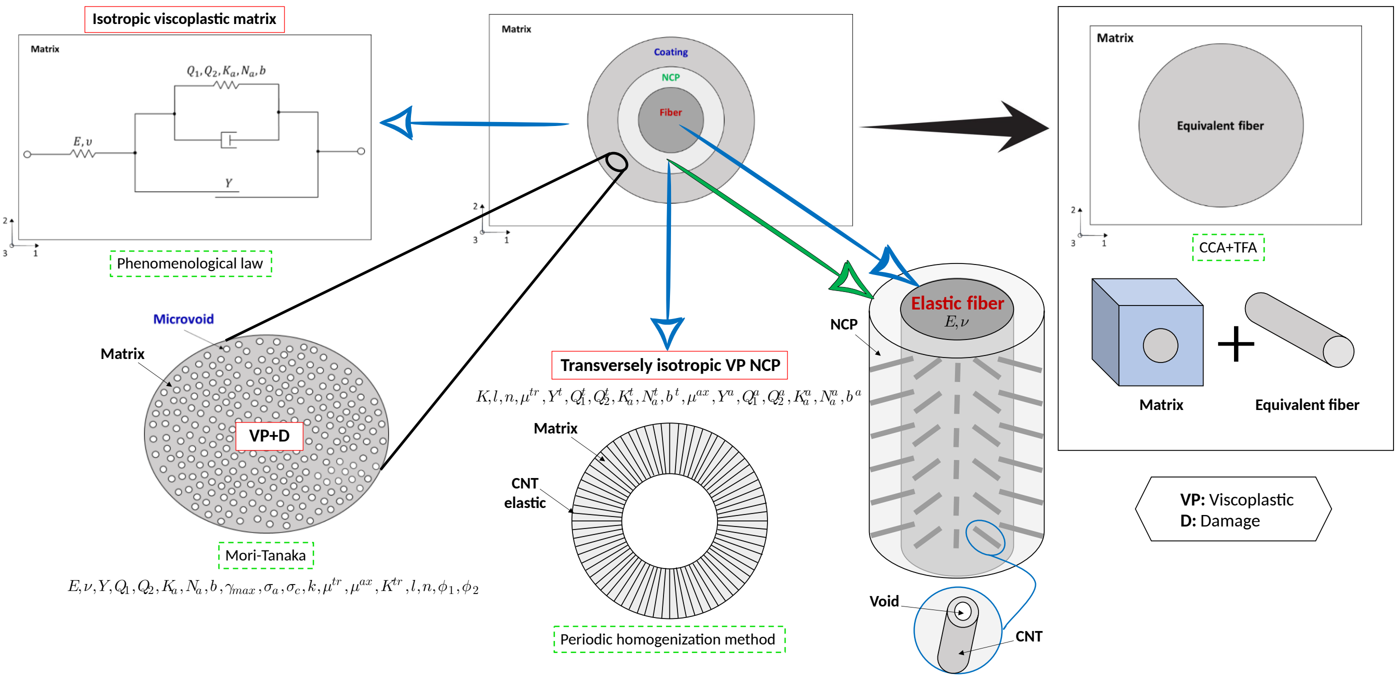
Isotropic viscoplastic matrix
Matrix
Q_1, Q_2, K_a, N_a, b
E, ν
Y
2
3
1
Phenomenological law
Matrix
Coating
NCP
Fiber
2
3
1
Matrix
Equivalent fiber
2
3
1
CCA+TFA
Matrix
Equivalent fiber
Microvoid
Matrix
VP+D
Mori-Tanaka
$E, \nu, Y, Q_1, Q_2, K_a, N_a, b, \gamma_{max}, \sigma_a, \sigma_c, k, \mu^{tr}, \mu^{ax}, K^{tr}, l, n, \phi_1, \phi_2$
Transversely isotropic VP NCP
$K, l, n, \mu^{tr}, Y^t, Q_1^t, Q_2^t, K_a^t, N_a^t, b^t, \mu^{ax}, Y^a, Q_1^a, Q_2^a, K_a^a, N_a^a, b^a$
Matrix
CNT
elastic
Periodic homogenization method
NCP
Elastic fiber
E, ν
Void
CNT
VP: Viscoplastic
D: Damage

Declaration of Interest Statement

Authors: I. Hanoun, G. Chatzigeorgiou, F. Meraghni:
Manuscript title: Hierarchical micromechanical modeling for CNT-coated fuzzy fiber composites accounting for viscoplasticity and interfacial damage

The authors declare that they have no known competing financial interests or personal relationships that could have appeared to influence the work reported in this article.

Metz, February 26, 2025